Computational Modeling and Bifurcation Analysis of Bubbling Fluidized Processes

by

Bing Zhu

A Dissertation submitted to the Faculty of Claremont Graduate University and San Diego State University in partial fulfillment of the requirements for the degree of Doctor of Philosophy in Computational Science

Claremont and San Diego, California
2008

Approved by:

Antonio Palacios, Co-Chair
San Diego State University

Peter Blomgren, Co-Chair
San Diego State University

We, the undersigned, certify that we have read this dissertation of Bing Zhu and approve it as adequate in scope and quality for the degree of Doctor of Philosophy.

Dissertation Committee:

Antonio Palacios, Co-Chair
Department of Mathematics and Statistics
San Diego State University

Peter Blomgren, Co-Chair
Department of Mathematics and Statistics
San Diego State University

Alpan Raval
Department of Mathematics
Claremont Graduate University

Ali Nadim
Department of Mathematics
Claremont Graduate University

Ricardo Carretero
Department of Mathematics and Statistics
San Diego State University

Abstract of the Dissertation

Computational Modeling and Bifurcation Analysis

of Bubbling Fluidized Processes

by

Bing Zhu

Claremont Graduate University and San Diego State University: 2008

Fluidization processes have many important applications in industry, in particular, in chemical, fossil, and petrochemical industries where good gas-solid mixing is required. Such mixing is commonly achieved through bubbles which are formed spontaneously and whose time-evolution appears to be governed by low-dimensional deterministic dynamics. Understanding the space and time dynamics in more detail is critical to future development of technologies that rely on the fluidization phenomenon—transport of solid particles by fluids—such as chemical reactors.

In response to this need, we use a low-dimensional, computational agent-based bubble model to study the changes in the global bubble dynamics in response to changes in the frequency of the rising bubbles. A computationally-based bifurcation analysis shows that the collective bubble dynamics undergoes a series of transitions from equilibrium points to highly periodic orbits, chaotic attractors, and even intermittent behavior between periodic orbits and chaotic sets. Using ideas and methods from nonlinear dynamics and time series analysis, we are able to approximate nonlinear models that allow for long-term predictions and the possibility of developing control algorithms. Additionally, we employ the Proper Orthogonal Decomposition to better understand the bubble dynamics generated by multiple injectors.

Acknowledgments

I am deeply grateful to my Ph.D. advisors, Professor Antonio Palacios and Professor Peter Blomgren, for their encouragement and invaluable ideas for finding methods and solutions to the numerous tasks involved in this thesis project. I also wish to thank Professor Ricardo Carretero for helpful discussions, and our research partners Sreekanth Pannala, Stuart Daw, and Charles Finney from Oak Ridge National Laboratory, for their ingenious work to make this project possible. I would also like to thank the joint Ph.D. program in the Computational Science Research Center at San Diego State University and Claremont Graduate University for the opportunity to receive such wonderful training in modern computational science. I also need to acknowledge the support of Reagan Moore, director of Data-Intensive Computing Environments group at the San Diego Supercomputer Center where I have worked full-time while pursuing my Ph.D. degree at SDSU and CGU.

Finally I would like to thank my parents, my wife, and my sons for their support in my journey to finish my Ph.D. degree, which has been my dream for many years.

Contents

List of Figures

Chapter 1

Introduction

Fluidization was introduced in fluid catalytic cracking processes to convert heavier petroleum cuts into gasoline in the early 1940s as the first large scale commercial application [28]. Today, fluidization processes have many important industrial applications, especially in chemical fossil and petrochemical industries where good gas-solid mixing is required. Typical industrial applications include: coal gasification, solid transportation, polymerization of olefins, heat exchange, polyethylene synthesis, cracking of hydrocarbon, catalytic reaction, water treatment, and nanotubes [6, 13, 15, 62]. Figure 1.1 depicts a schematic picture of a large circulating fluidized combustor in Florida, in which upward blowing air lifts solid fuels, providing a turbulent mixing of gas and solids.

The application of fluidized bed reactors in industries has specific advantages such as providing excellent gas-solid contacting and particle mixing [6], rapid heat exchange through circulating solids and easy control due to liquid like behavior [11]. On the other hand, fluidized-bed reactors have disadvantages such as insufficient contact among gas and solids due to bubbling in a fluidized bed which consumes too much energy in circulating gas [46], gas-bypassing in the form of bubbles, jets and channeling.

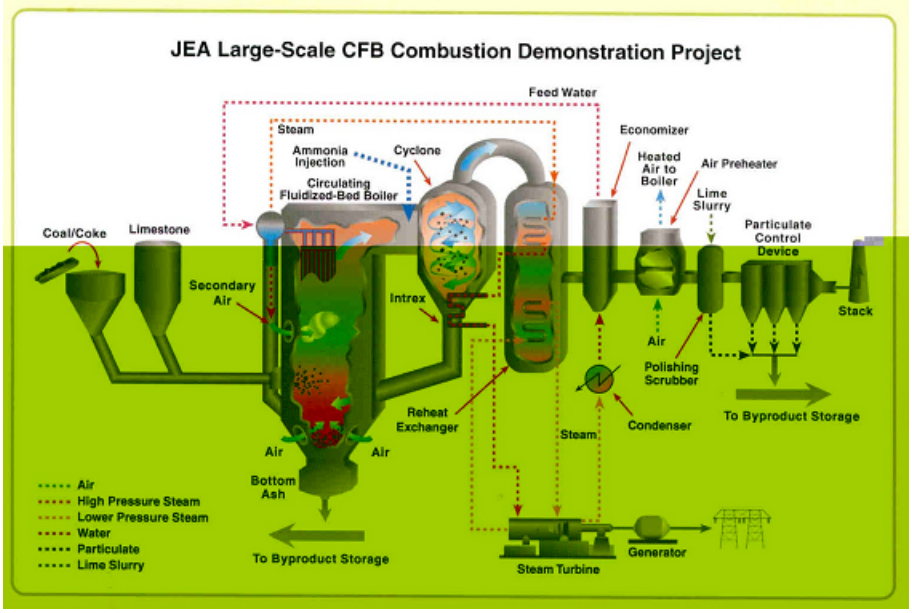

Figure 1.1: Application of a Circulating Fluidized Bed combustor to generate electric energy (courtesy of DOE/National Energy and Technology Laboratory). Upward blowing air lifts solid fuels, providing a turbulent mixing of gas and solids.

The behavior of a fluidization process can have numerous regimes based on the size of the fluidized bed, flowing medium, flow velocity, physical properties of the solid particles, and operating conditions [25, 62]. Bubbling is an important phenomenon existing in most fluidization processes in which bubbles are generated continuously, move upward vigorously, coalesce and interact with the flowing medium and particles [6]. In applications in chemical, fossil and petrochemical industries, excellent gas-solid mixing are even achieved through bubbles that are spontaneously formed during the fluidization processes. Therefore, it is necessary to have good understanding of fluidization processes, especially of the bubble dynamics, to provide reliable control mechanisms for the wide range applications in industry. One important research direction, which we adopt in this project, is to study the sensitivity of the bubble hydrodynamics as well as of fluidization processes in response to small perturbations of some key parameter(s), such as bubble injection frequency.

To do so, we use a low-dimensional, computational agent-based model of bubble behavior, to study the changes in the global dynamics of the bubbles in response to changes in the frequency of the rising bubbles. A computationally-based bifurcation analysis shows that the collective bubble dynamics undergoes a series of transitions from equilibrium points to highly periodic orbits, chaotic attractors, and even intermittent behavior between periodic orbits and chaotic sets. Using ideas and methods from nonlinear dynamics and time series analysis, we are able to approximate nonlinear models that allow for long-term predictions and the possibility of developing control algorithms. Additionally, we employ the Proper Orthogonal Decomposition to better understand the bubble dynamics generated by multiple injectors.

The material in this thesis is organized as follows.

In Chapter 2, we start with a review of the nature of fluidization processes based on previous experiments, including the description of three principal thresholds of fluidization velocities: minimum fluidization velocity, minimum bubbling velocity, and terminal velocity. Then we explore the main issues regarding bubble dynamics, including bubble shapes, bubble-bubble interactions, velocity of a single rising bubble, and a popular two-phase model for the formation of bubbles. We also discuss in this chapter the emulsion phase, which is a mixture of gas and fine particles and is another focus for this research project besides bubble dynamics.

The difficulty of modeling three-phase gas-solid-bubble dynamics in a fluidized bed lies mainly in modeling bubbles and their complex dynamical behavior, including coalescence and splitting [8]. Determining the velocity of each bubble is an essential part in the modeling task. In Chapter 3, we introduce a low-dimensional, agent-based bubble model, known as *Dynamic Interacting Bubble Simulation* (DIBS), which describes main bubble-bubble interactions based on empirical observations and data

fitting techniques such as imaging methods. We also summarize other approaches for modeling the spatio-temporal behavior of bubbles and give critical reviews of these models and their comparison to our DIBS bubble model.

With large amount of fine particles, both gas and solids can be treated as continuum flows and thus can be modeled using traditional computational fluid dynamics (CFD) methods. In Chapter 3, we present a review of CFD-based modeling using the continuity equation for mass conservation and Navier-Stokes equation for momentum conservation, as well as a quick review of boundary conditions. Since our focus is on the emulsion phase and bubble phase, we develop a computational scheme for numerical simulation of emulsion phase via finite difference methods.

Our main contributions in this thesis project are located in Chapters 4, 5, and 6, where we develop efficient data analysis techniques, bifurcation analysis, and time series analysis, to study the global bubble dynamics in bubbling fluidized beds in response to small perturbations of some bifurcation parameter(s) for the purpose of providing control techniques or mechanisms in industrial applications. In Chapter 4, we use the low-dimensional DIBS model to study the changes in the global dynamics of fluidized beds by varying the bubble injection frequency, which is considered as a distinguished bifurcation parameter.

This study is related not only to the control of fluidized beds but also to more fundamental questions regarding the generation and transmission of information and self-organization in spatio-temporal systems. Our study is aimed at the relatively simple case of centralized single bubble nozzle. Other data analysis methodologies are mainly based on the theory of time series analysis, including phase-space embedding techniques, phase-portrait reconstruction, and data model fitting for future data prediction. Our bifurcation analysis reveals that the bubble dynamics is attracted to-

wards a fixed point at low frequencies, then evolves into a series of bifurcations with new behaviors, including a single chaotic attractor, highly periodic orbits, multiple chaotic attractors, and intermittent behavior between periodic orbits and chaotic sets. By applying the time series analysis techniques, we demonstrate that the nonlinear bubble dynamics can be reconstructed using local linear fitting model for long-term prediction for all bubble injection frequencies, except for the region that exhibits intermittent behavior. The computational approaches of the time series analysis are also described in greater detail in these chapters. In Chapter 4, in particular, we implement a computational approach to numerically estimate the maximum Lyapunov exponents. The results are consistent with the complex transitions shown by our bifurcation analysis.

In Chapter 5, a different data analysis method, the Proper Orthogonal Decomposition (POD), is used to extract the dominant features of computer simulations of bubble dynamics with multiple injectors and of experiments with a spouting bed. We present a method to digitize frames of data for a fluidized process and apply the POD decomposition to extract dominant spatial features and unravel the temporal evolution of the bubble dynamics. The temporal evolution data obtained through the POD technique discloses different dynamical regimes of bubble swarms in fluidized processes as bubble injection frequency varies. It is also found, however, that it is rather hard to identify a few dominant components for the case with multiple bubble injectors. In spite of this shortcoming, the POD analysis was successfully applied to spouting beds, yielding around 20 modes to sufficiently capture 80% of the total energy in its overall dynamic behavior.

In Chapter 6, we present a revised version of the DIBS model that includes the emulsion phase. This revised model includes coupling for bubble phase and emulsion phase, meaning that bubbles impact the emulsion phase through volume fraction while

the emulsion phase affects the rising velocities of the bubbles. With this new model, we revisit our bifurcation analysis with single nozzle and compare the results between the original DIBS simulation from Chapter 3 and the revised bubble-emulsion model. We also carry out simulations with the revised computational model to compute the ozone concentrations and compare simulations with the data from real fluidized bed experiments by Fryer *et al.* and the data from the original DIBS model by Pannala *et al.* The results show a fairly good match for various gas superficial velocities.

Chapter 2

Background

2.1 Fluidization Processes

Fluidization is a process in which solid particles behave like liquid in a vessel due to a continually flowing medium such as gas or air [25, 30, 31, 32]. A fluidized bed, regardless of its application, normally consists of a vessel that contains solids and has a porous bottom plate for injecting a flowing medium upward. When the flow rate is low, the flowing medium percolates through the gaps between the particles. The particles remain packed and are in a steady state as is shown in Figure 2.1(a). As the flow speed of the medium increases and reaches a threshold at which the forces from the flow exerted on the particles overcome gravitational forces, particles start to be suspended in the flowing medium inside the vessel. Further increasing the flow speed will cause particles to behave like fluids, a state called fluidization (see Figure 2.1(b)). This threshold of flowing velocity for the carrying medium is called the minimum fluidization velocity (U_{mf}). Many efforts have been made to find a formula for the correlation between minimum fluidization and physical properties of the flowing medium and particles for the purpose of providing accurate design in building a fluidized bed. For a complete list of the formulas, see [15].

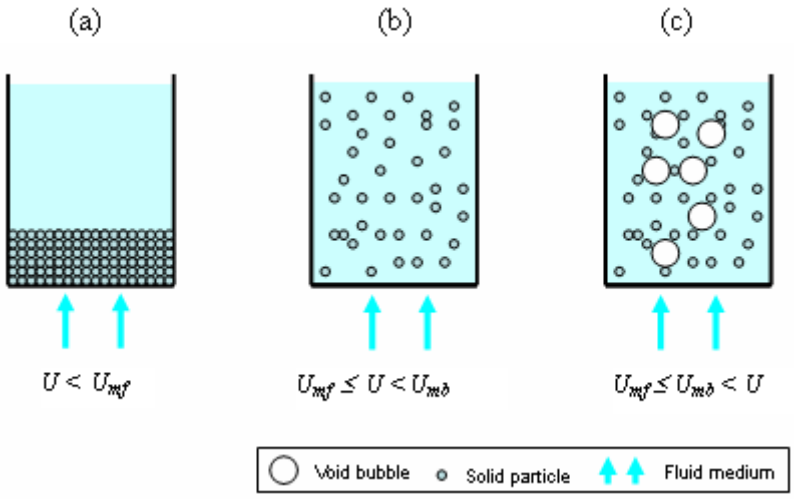

Figure 2.1: Fluidization Processes. (a) Fluidized bed is in a steady state when the upward flow rate, U, is less than the minimum fluidization velocity (U_{mf}). (b) Fluidization happens when the flow rate crosses U_{mf}. (c) When the flow rate reaches the minimum bubbling velocity (U_{mb}), bubbles are created and the fluidized bed exhibits three phases, bubble phase, solid phase and gas (or liquid) phase.

As the flow rate increases further towards a second threshold, called the minimum bubbling velocity (U_{mb}), bubble voids are formed thus creating a dramatic change in the dynamics as bubbles move upwards vigorously and coalesce when bubbles touch. Figure 2.1(c) illustrates a fluidized bed with medium flow, moving particles, and bubbles. This particular state is the bubbling fluidized regime and is the focus of the work in this thesis. Our goal is to seek computational solutions and bifurcation analysis methodologies that can help us understand the spatio-temporal behavior of bubbles, their interactions with solid particles and gas, and transitions between different dynamical regimes in response to changes in parameter(s).

A bubbling fluidized bed has three phases: bubble phase, solid phase and gas (or liquid) phase as illustrated in Figure 2.1(c) [24]. The dynamics of such three-phase fluidized bed varies depending on the bed design, particle size and shape, density and cohesiveness [25, 62]. With modern technologies, scientists and researchers have been using imaging system such as Capacitance Imaging Systems used by Halow and

Nicoletti [34], Particle Image Velocimetry (PIV) by Chen and Fan [12], and X-ray computational tomography by Behling and Mewes [3], to gather empirical information of fluidization process from actual experiments. Numerical work based on computational fluid dynamics (CFD) methods allows integration of computer simulation and visualization tools to obtain numerical solutions of available models that can provide insight into the complex interactions that occur during the fluidization phenomenon [24, 31, 32].

2.2 Bubble Dynamics in Fluidized Beds

An often observed regime in fluidization is bubbling in which bubbles are generated from the granular bottom of a fluidized bed and rise vigorously. In the bubbling fluidized regime, bubbles are generated as the speed of the flowing medium reaches the minimum bubbling velocity. Due to the upward moving flowing medium and buoyancy, the rising velocities of bubbles are closely related to physical properties of a fluidized bed such as the viscosity of the flowing medium and particles. Thus the flow of bubbles creates a complex dynamical system in the bubbling fluidized regime that can be a key factor in determining the system hydrodynamics [24].

The shape of a bubble in a fluidized bed is mainly controlled by its surrounding solids and flowing medium. For small bubbles, the bubble shape is almost spherical due to the dominance of surface tension. When a bubble has an intermediate size, its shape tends to be oval with a sphere cap. Bubbles become slugs when they are large. The shape of a slug can be a round spherical cap with a flat bottom like a bullet or is like a half bullet when a slug is attached to the bed wall [15, 46].

There are two main bubble-bubble interactions. One is bubble coalescence, which is the most prevalent in bubbling three-phase fluidized beds [50]. When two bubbles

touch physically in three-dimensional space, they tend to coalesce quickly as observed in fluidized-bed experiments by Toei and Matsuno in 1967 [73], Shichi *et al.* in 1968 [69], Clift and Grace in 1970 [14] by using photographs and tracing techniques, and by Halow and Nicoletti in 1991 using capacitance imaging systems [34]. Another important bubble-bubble interaction is that in which a bubble exerts some pulling force on its trailing bubble and thus changes the bubble rising velocity of the trailing bubble [18, 60]. These two main features in bubble dynamics are included in the computational bubble model we adopted in our work which will be described in more detail in Chapter 3.

Fan [24] proposed a bubble break-up model in which he claimed that the bubble-particle collision is the reason for a bubble to break. The bubble-particle collision causes either the bounce of the particle away from a bubble or the penetration of a particle into the bubble, which can cause bubble break-up. Clift *et al.* [14] presented three crucial factors that can cause bubble break-up. Thus in the case of fine particles such as powders, bubble break-up is almost impossible and so far is not included in the DIBS bubble model.

Davies and Taylor [16] presented the first formula in 1950 to estimate the rise velocity of a single bubble:

$$V_{b\infty} = (2/3)\sqrt{gR}, \tag{2.1}$$

where g is the gravitational acceleration and R is the bubble diameter. This is an oversimplified formula when dealing with a cluster of rising bubbles. Werther [78] found that the velocity of a rising bubble is also related to the bed diameter. In an actual fluidized bed with a cluster of bubbles, the velocity of each bubble increases with bubble concentration [13]. Thus the interactions for a bubble with other bubbles must be included. For an array of bubbles in a bubbling fluidized bed, the velocity

of a bubble can be generically expressed as:

$$\vec{V_k} = V_{b\infty}\vec{i} + \vec{Q}_k, \tag{2.2}$$

where $\vec{V_k}$ is the velocity of bubble k, $\vec{i}$ is the unit vector in the vertical direction, and $\vec{Q}_k$ is the additional velocity of the bubble k from the interaction with other bubbles. In Chapter 3, we present several approaches for modeling bubble velocities.

The two phase model by Toomey and Johnstone [74] proposed that bubble volume is proportional to excess velocity, which is the difference between bubble superficial velocity and minimum fluidization velocity in their two-phase theory. Based on this assumption, a low-dimensional model, *Dynamic Interacting Bubble Simulation* (DIBS) model, was developed by Pannala *et al.* at Oak Ridge National Laboratory in Tennessee [35, 58]. The DIBS model identified the leading bubble as the most influential one in determining the velocity of a trailing bubble in a fluidized bed. The DIBS formula for bubble velocity in bubbling gas-solid fluidized beds was derived empirically through imaging system and is discussed in greater detail in Chapter 3.

2.3 Emulsion Phase

In the three-phase bubbling fluidized regime, the motion of the flowing medium impacts the movement of bubbles and particles. Different flow regimes of gas (or liquid) phase and particle phase will be present depending on the design of the fluidized bed. The main factors are gas (or liquid) flow velocity, solid particle size, shape and density, and actual operating conditions.

Figure 2.2(a) illustrates a circulating fluidized bed in which solids are collected and then are circulated back into the fluidized bed. In this fluidized bed, upward flow and movement of particles are quite homogeneous.

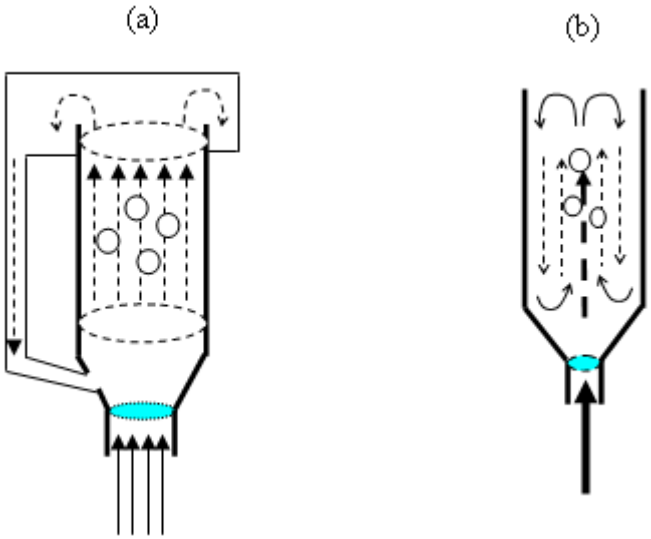

Figure 2.2: Fluidized Beds. (a) A circulating fluidized bed which has upward flow of bubbles and circulating emulsion phase. (b) A spouting bed circulates solids through a single centralized jet.

Figure 2.2(b) shows a spouting bed in which solids circulate inside the bed by gas through a single centralized jet, creating a complicated three phase bubbling fluidized regime.

When there is a large number of fine particles such as fine powders or catalysts, gas (or liquid) and fine particles are mixed together to form the emulsion phase. Bubbles (void spaces) rise much faster than the upward flowing gas in emulsion phase, promoting circulation and mixing of particles. In such a fluidized bed, only two phases, bubble phase and emulsion phase, need to be considered. When the flowing medium is liquid, the emulsion phase is the liquid-like flow after mixing with particles and thus can be easily distinguished from air bubbles. In a gas-solid fluidized bed, the excessive flow, reaching minimum bubbling velocity, passes through the fluidized bed and creates void spaces that behave like air bubbles and have been observed in actual experiments. This forms the basis for the two-phase theory by Toomey and Johnstone [74]. Using capacitance imaging system, Halow and Nicoletti [34] observed

that there is a grey region between a voidage (bubble) and emulsion phase, indicating there are no sharp boundaries for voids in a gas-solid fluidized bed. This grey region is also referred to as a cloud and we will discuss it in Section 6.3 for calculating ozone concentrations.

Chapter 3

Computational Modeling of Bubbling Fluidized Processes

3.1 DIBS - A Low-dimensional Bubble Model

Since the time when Davies and Taylor [16] introduced Eq. (2.1) for the velocity of a free rising bubble in a bubbling fluidized bed in 1950, many attempts have been made for modeling bubble velocities. Earlier work focused mainly on explaining bubble formation and the physical properties such as bubble diameter, size, and shape. Harrison and Leung [36], Zenz [79], and Caram and Hsu [10] developed various models that described the growth of bubbles due to gas injection at a single orifice. Nieuwland *et al.* [54] provided a complete review of existing models in 1996. However, none of these efforts addressed the collective behavior of bubbles nor the complete interactions, in space and time, which were commonly observed in related experiments.

With the arrival of modern computers, scientists and engineers started to develop computational models and numerical simulations of bubble dynamics. The CHEMFLUB software developed by Systems Science and Software Inc. in 1980 presented one modeling approach to simulate gas and solids flow in fluidized gasifiers [4, 30, 63, 66].

In its approach, bubbles are treated as a continuum flow and thus the continuity equation is applied to model the bubble column. Yet the complicated phenomena of bubbles in bubbling fluidized beds, for example, the bubble-bubble interactions including bubble coalescence, are missing in such a computational model. Developing visualization software to simulate and trace trajectories of bubbles from such an approach is also difficult. Thus a discrete bubble modeling (DBM) method, in which the motion of each bubble is traced computationally by solving a modeling equation along with additional models for bubble coalescence and bubble splitting, provides a more accurate approach.

In recent years, Kuipers *et al.* [7, 22] have been actively working on a direction to model bubble dynamics using a Newtonian approach. In their approach, each bubble is modeled as an individual agent described via a Newtonian equation of the form:

$$m_b \frac{dv}{dt} = \Sigma F, \quad \Sigma F = F_g + F_p + F_d + F_{vm}, \tag{3.1}$$

where m_b is the mass of a bubble, v is its velocity, and F is the total force acting on the bubble, F_g is the gravitational force, F_p is the pressure force, F_d is the drag force from the flow resistance towards a moving bubble, and F_{vm} is the virtual mass force from the acceleration of the emulsion phase. The advantage of Kuipers' DBM approach is that it has solid theoretical foundation and can have two-way coupling integration with the computational model of the emulsion phase.

Lapin *et al.* [47] presented a different DBM model in 2001 for bubble velocity in which they claimed the bubble motion was drawn by pressure gradients and was decreased by its flow resistances. They came up with the following equation for bubble velocity:

$$c_{vm}\rho_L \frac{d\mathbf{u}_{slip}}{dt} = -\nabla p - c_d \mathbf{u}_{slip}, \tag{3.2}$$

where $\mathbf{u}_{slip}$ is the bubble velocity, c_{vm} is the virtual mass coefficient, ∇p is the pres-

sure gradient, ρ_L is the fluid density, and c_d is the drag coefficient. Godo [33] used Lapin's bubble model and presented the same idea as ours regarding two-way coupling between bubble and emulsion phases as we will discuss this in Chapter 6.

However, both approaches totally ignore the important acceleration factor for a rising bubble from its leading bubble, which has been observed in actual experiments.

In the 1980s, scientists and researchers began to use imaging systems to study the dynamics of bubbles in fluidized beds. Among those works, Halow and Nicoletti used capacitance imaging system, consisting of electronic sensing circuits and electrodes, to record the discretized images in three dimensions of the voidage distributions inside a fluidized bed [34]. In 1993, Halow *et al.* presented an empirical formula for the velocity of a rising bubble that took into account the fact that a bubble has some pulling force for a trailing bubble [35]. This work laid the foundation for the computational model for bubble dynamics in fluidized bed, *Dynamic Interacting Bubble Simulation*, or DIBS model, which was developed in 2001 jointly by Pannala, Daw, and Halow [20, 57, 58, 59] at Oak Ridge National Laboratory, Tennessee. The name of the DIBS model was officially introduced for the first time in 2004.

3.1.1 Bubble Rise Velocity

In a bubbling fluidized process, bubbles move rapidly upward and particles flow around rising bubbles. For a single bubble, the volume balance between the solid flow and bubble movement forms the following relation for the solids velocity and bubble rising velocity:

$$U_s = \frac{A_b}{A_e} \cdot \frac{1-\epsilon_w}{1-\epsilon_e} \cdot U_b, \tag{3.3}$$

where U_s is the velocity of the solid phase, U_b is the bubble rising velocity, A_b is the area of cross section of the bubble, A_e is the area of emulsion phase, ϵ_w is the void

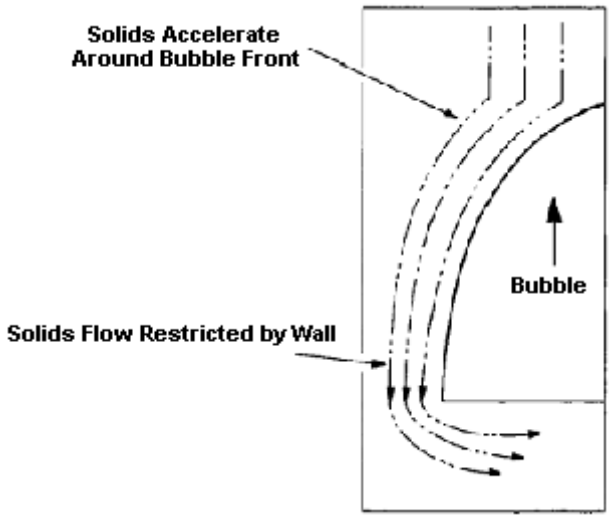

Figure 3.1: Schematic diagram of a rising bubble and its interaction with surrounding solids flow by Halow and Nicoletti.

behind the bubble, and ϵ_e is the void in the emulsion phase surrounding the bubble. Notice that $A_e = A_t - A_b$, where A_t is the area of the cross section of the fluidized bed.

For the flow of particles, Bernoulli's equation generates the relation

$$l_b = \frac{{U_s}^2}{2g} + \frac{{V_s}^2}{2g}, \tag{3.4}$$

where l_b is the length of a bubble, g is the gravity acceleration, and V_s is the solids velocity tangent to the nose of a bubble (See Figure 3.1). If we assume the nose of the bubble to be hemispherical, V_s and U_b have the following relation:

$$V_s = \frac{1}{\sqrt{2}} \left(\frac{D_b}{l_b} \right) U_b, \tag{3.5}$$

where D_b is the diameter of the bubble.

Taking an approximate form for Eq. (3.3) by considering both ϵ_w and ϵ_e to be $\epsilon_{-\infty}$, *i.e.*, the voidage in the emulsion phase far from the bed, and then combining

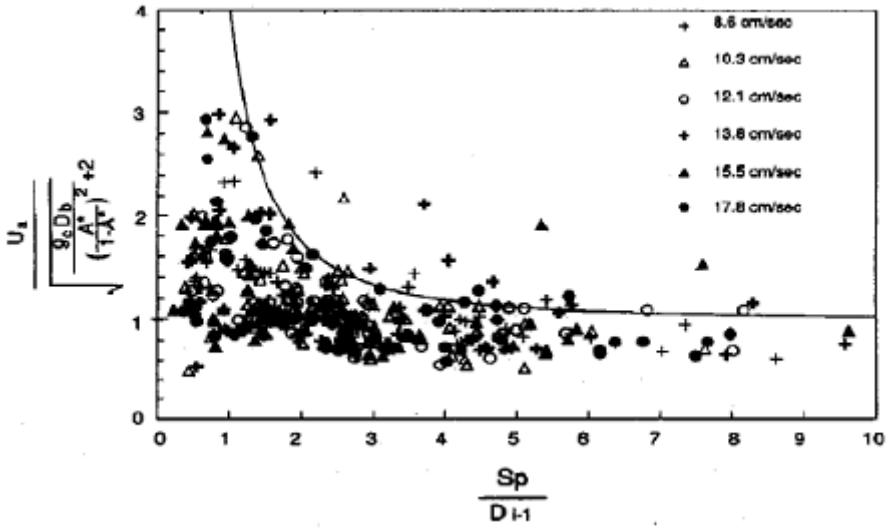

Figure 3.2: Collected velocity data of a trailing bubble from imaging system and fitting curve from Eq. (3.7) by Halow and Nicoletti. The final equation (3.8) used in the DIBS model is empirically revised based on Eq. (3.7).

the results of Eq.(3.4) and Eq.(3.5), the rising velocity of a bubble can be written as:

$$U_b = \sqrt{\frac{gl_b}{2 + \left(\frac{A^*}{1 - A^*}\right)^2}}, \tag{3.6}$$

where $A^* = A_b/A_t$, the ratio of bubble cross section area to bed area.

The imaging system for the bubbling fluidized bed captures bubble wake behavior that exerts some pulling force and accelerates the rise of a trailing bubble. This is an additional velocity for a bubble that is trailing another bubble and is related to the diameter of its leading bubble. Figure 3.2 is a plot by Halow and Nicoletti illustrating actual experimental data and a fitting curve from the following empirical formula for a trailing bubble:

$$U_b = \sqrt{\frac{gl_b}{2 + \left(\frac{A^*}{1 - A^*}\right)^2}} \left[1 + 3\left(\frac{D_{i-1}}{S_p}\right)^2\right], \tag{3.7}$$

where D_{i-1} is the diameter of the leading bubble and S_p is the distance between a trailing bubble and its leading bubble.

In 1993, Halow and Fasching [35] further examined their fitting model. By comparing Eq. (3.7) with those by Farrokhalaee [27] and Lord [49], they suggested that the square term be replaced by a cubic form. This established the bubble velocity formula of Eq. (3.8) adopted by Pannala, Daw, and Halow who later developed the computational DIBS model [60] for bubble dynamics in bubbling fluidized bed.

3.1.2 Computational DIBS Model

The DIBS model was officially introduced in 2004 by Pannala *et al.* [58]. In the DIBS model, each bubble is treated as a single agent and is described by a low-order ordinary differential equation (ODE):

$$\left\| \frac{d\vec{X}_i}{dt} \right\| = \|\vec{V}_i\| = \sqrt{\frac{gl_i}{2 + \left(\frac{A_i^*}{1 - A_i^*} \right)^2}} \left[1 + 3 \left(\frac{D_{Lj}}{X_{i-j}} \right)^3 \right], \tag{3.8}$$

referring to Figure 3.3, $\vec{X}_i$ is the position, $\vec{V}_i$ is the velocity, l_i is the length of i-th bubble, A_i^* is the fraction of cross section area of i-th bubble divided by testbed area, D_{Lj} is the diameter of the leading bubble, and X_{i-j} is the distance between i-th bubble and its leading bubble, j-th bubble.

Besides Eq. (3.8) for each bubble, there are some assumptions in the computational DIBS model.

i. If a bubble does not have a leading bubble, its equation will be the one having no j related term, *i.e.* the cubic term, in Eq. (3.8).

ii. Each bubble is spherically shaped if the diameter of the bubble is less than 85% of the bed diameter. If the diameter of a bubble is larger than or equal to 85%

of the bed diameter, the bubble will be cylindrically shaped with a hemispherical end cap.

iii. At any moment, the movement of a bubble is affected by its leading bubble through a pulling force. A bubble j is called a leading bubble for a bubble i if the bubble j has vertical position above the bubble i and has the shortest distance with the bubble i (See Figure 3.3).

iv. Two bubbles coalesce when they touch in 3-dimensional space.

v. When reaching testbed surface, a bubble disappears.

vi. The bubble rise velocity given by Eq. (3.7) is relative to the solid flow in the fluidized bed.

Notice that by assumptions (iv) and (v), the number of ODEs varies as the number of bubbles changes with the fluidized bed. Thus, it is very difficult to carry out an analytic study of this model purely by looking at a cluster of coupled bubbles modeled by Eq. (3.8). On the other hand, the use of powerful computers allows such computational model to be implemented numerically and simulated graphically. Figure 3.4 is a modified version of a flowchart for the implementation of the DIBS model originally designed and implemented by Pannala *et al.* at Oak Ridge National Laboratory [60].

In assumption (i), the DIBS model stresses the influence of an immediate leading bubble for bubble velocity. It is also worth mentioning that such approach was sought in the early 1970s by Orcutt and Carpenter [55] in 1971, and Allahwla [1] in 1975.

In the actual computational simulation, bubbles are generated periodically from a fixed number of bubble injectors through a porous plate located at the bottom of a fluidized bed. The bubble injection frequency will play an important role in our

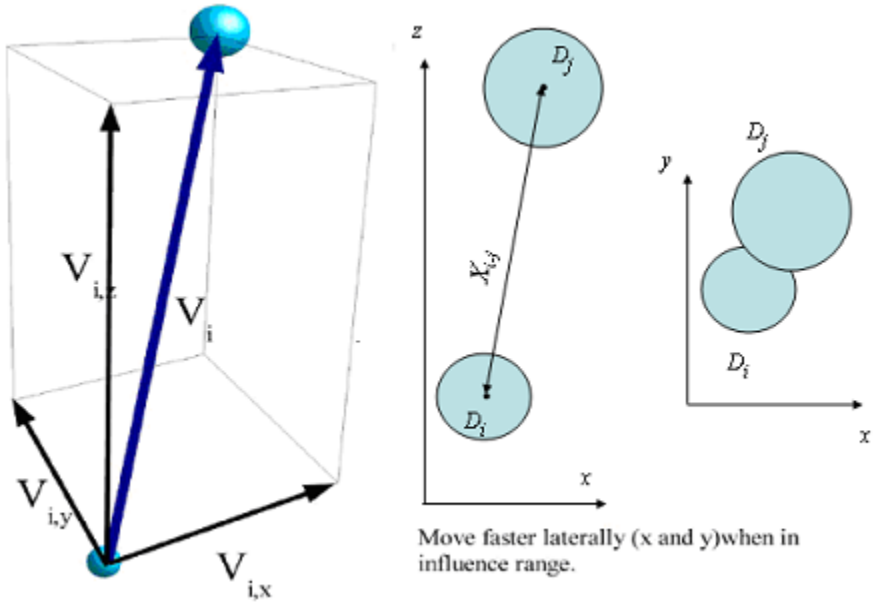

Figure 3.3: The leading bubble j exerts a pulling force on a trailing bubble i. Bubble j is the leading bubble for bubble i if bubble j is above bubble i and has the shortest distance between two bubble, X_{i-j}.

bifurcation analysis, as it will be discussed later in Chapters 4 and 5. The initial critical values for the DIBS simulation are the bed shape (either a cylindrical or a rectangular test bed), bed size, the number and positions of bubble injectors, bubble injection frequency, minimum fluidization velocity, and superficial velocity of the gas flow. A detailed list of initial values of our computational simulation are listed in table 4.1 in Chapter 4.

The operation to update locations of bubbles is to numerically solve Eq. (3.8) for each bubble. The first order Euler method can be used with a small value of integration time step size to acquire better accuracy in finding numerical solutions. After the bubble-positions are updated, the program checks the boundary condition in the sense that a bubble is bounced fully when it meets the side wall of the vessel. The program then checks if there are coalescing bubbles by checking if there are two bubbles that are physically in contact with one another. Bubbles that touch

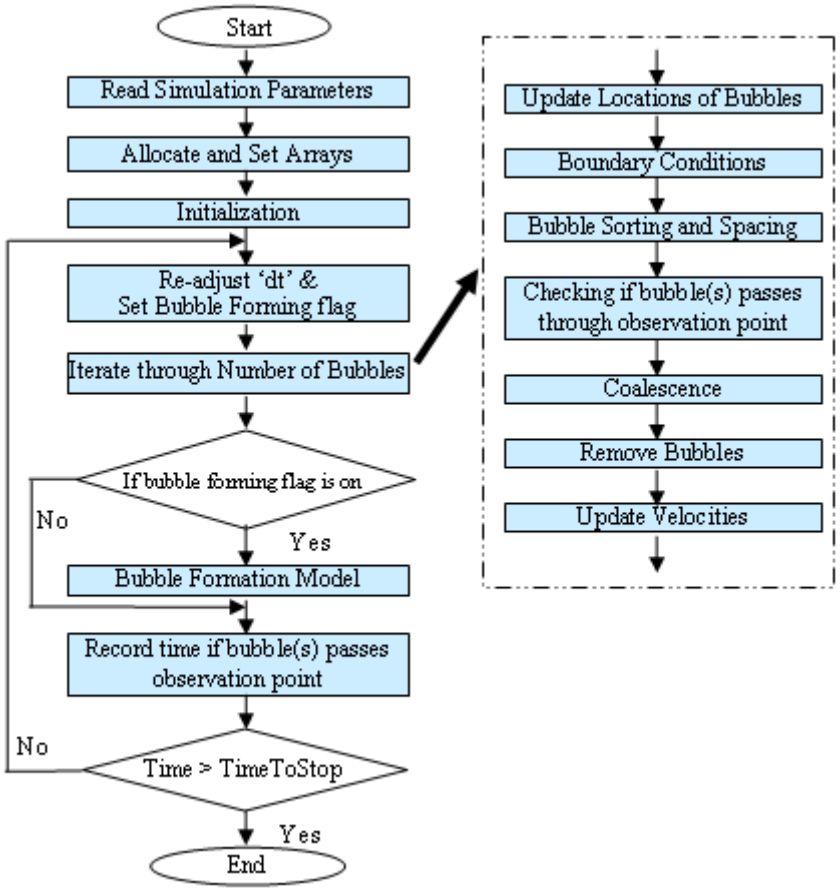

Figure 3.4: The modified flowchart of computational simulation of DIBS model with adaptive integration step size. The operation to update the locations of bubbles is actually to numerically solve the ODE of Eq. (3.8).

in 3-dimensional space are merged into one bubble with volume equal to all merged bubbles. Bubbles that surpass the top of the fluidized bed are removed from the computational array.

Bubbles are generated periodically in a real-time simulation in which the software program checks at each loop if it is time to generate new bubbles. New bubbles are formed with a fixed bubble diameter, or with an initial size related to gas velocity, from the bottom of the fluidized bed and are then added into the bubble array. Each bubble has an initial color that is changed once it passes a fixed observation point. If there is a new bubble or bubbles passing the observation point, the passage time is

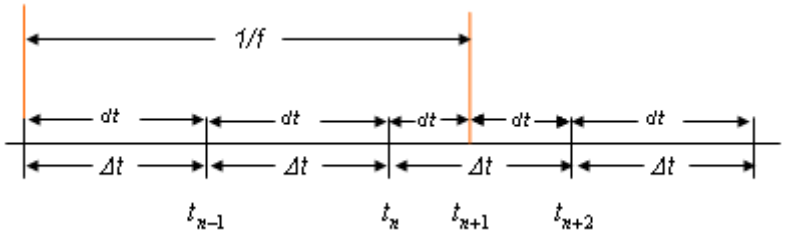

Figure 3.5: Adjustable dt for ODE integration. Δt is the initial fixed time step size. f is the bubble injection frequency. And dt is the adjustable time step size. An extra integration step is taken at t_{n+1}.

recorded for further bifurcation analysis that is described in more detail in Chapter 4.

After each computational loop, the time is advanced to the next time step. Usually the time step size is fixed in a finite difference method to find numerical solutions of differential equation(s). However, we realized that the actual integration time step size, dt, has to be adjusted in real-time to be able to run the simulations with bubble injection frequency (BIF) values that are evenly distributed in a given interval. This is because there would be limited choices of BIF values if the fixed value of dt is used due to the following relationship:

$$f = \frac{1}{N \cdot dt}, \tag{3.9}$$

where N is the number of time steps between two bubbles to be generated and f is the bubble injection frequency (BIF). If a fixed $dt = \Delta t$ is used, the values of f from Eq. (3.9) would not be evenly distributed on any given interval by varying N as positive integers. To overcome this problem, a variable integrating time step, dt, is used in actual implementation. The value of dt is checked and adjusted as needed in each loop as illustrated in Figure 3.5. With this approach, values of BIFs for the simulations can be evenly distributed in any given interval, thus allowing us to carry bifurcation analysis for bubble dynamics in response to changes in injection frequencies.

3.2 Modeling Gas and Particle Phases

Two fundamental modeling approaches, Eulerian-Eulerian and Eulerian-Lagrangian, are used to model multiphase flows for gas phase and particle phase. The Eulerian-Eulerian is a continuum based modeling method in which each phase is treated as a flow. The Eulerian-Lagrangian approach seeks modeling for each individual particle and thus is able to simulate trajectories of dispersed particles.

Using the Eulerian-Lagrangian approach, a complete description of the dynamics of solid particles suspended in a Newtonian fluid can be achieved through the Navier-Stokes equations for the fluid phase and the Newtonian equations for the solids. This approach, however, leads to solving a very large number of equations at each time step in order to trace the movement of all particles in a fluidized bed. When the number of particles is very large, finding a numerical solution becomes so computationally intensive that it can easily exceed the computing power of any of today's supercomputers, not to mention handling the particle-particle and particle-gas interactions. Therefore, it is suitable to use a granular flow model, namely the Eulerian-Eulerian approach, to model both gas and particle phases for practical purposes.

When pursuing the Eulerian-Eulerian approach for gas and particle phases, the popular computational fluid dynamics (CFD) method can be applied to describe both gas and particle phases mathematically, in which the well-known Navier-Stokes equations and continuity equations are used based on the fundamental laws of conservations of momentum and mass [24, 31, 32, 51, 52].

3.2.1 Governing Equations

Conservation of Mass

Gas Mass Balance:

$$\frac{\partial}{\partial t}(\epsilon_g \rho_g) + \nabla \cdot (\epsilon_g \rho_g \vec{v}_g) = 0, \tag{3.10}$$

Solid Mass Balance:

$$\frac{\partial}{\partial t}(\epsilon_s \rho_s) + \nabla \cdot (\epsilon_s \rho_s \vec{v}_s) = 0, \tag{3.11}$$

where, with respect to gas and solids by the corresponding subscripts, ϵ_g and ϵ_s are volume fractions, ρ_g and ρ_s are densities, and $\vec{v}_g$ and $\vec{v}_s$ are velocities.

Conservation of Momentum

Gas Momentum Balance:

$$\frac{\partial}{\partial t}(\epsilon_g \rho_g \vec{v}_g) + \nabla \cdot (\epsilon_g \rho_g \vec{v}_g \vec{v}_g) = -\epsilon_g \nabla P + \nabla \cdot \bar{\bar{\tau}}_g + F_{gs}(\vec{v}_s - \vec{v}_g) + \epsilon_g \rho_g \vec{g}, \tag{3.12}$$

Solids Momentum Balance:

$$\frac{\partial}{\partial t}(\epsilon_s \rho_s \vec{v}_s) + \nabla \cdot (\epsilon_s \rho_s \vec{v}_s \vec{v}_s) = -\epsilon_s \nabla P + \nabla \cdot \bar{\bar{S}}_s + F_{gs}(\vec{v}_g - \vec{v}_s) + \epsilon_s \rho_s \vec{g}, \tag{3.13}$$

where P, $\bar{\bar{S}}_s$ and $\bar{\bar{\tau}}_g$ represent pressure in the gas phase, solid phase stress tensor, and fluid phase deviatoric stress tensor. F_{gs} denotes the coefficient of the interface force between gas phase and solid phase, and $\vec{g}$ is the acceleration due to gravity.

In the case of the emulsion phase, the equations are reduced to two equations, one equation for conservation of mass and another equation for the conservation of energy. The DIBS model is coupled with the equations for the emulsion phase. More precisely, bubbles impact the emulsion phase in the sense that bubbles are used to compute the volume fractions in both equations of mass conservation and energy conservation for emulsion phase. With this coupling, a generic computational program can be constructed as depicted by the flowchart in Figure 3.6.

The boundary conditions for the governing equations of gas and particle phases, including bed wall, inlet and outlet of a fluidized bed, vary depending on actual flow

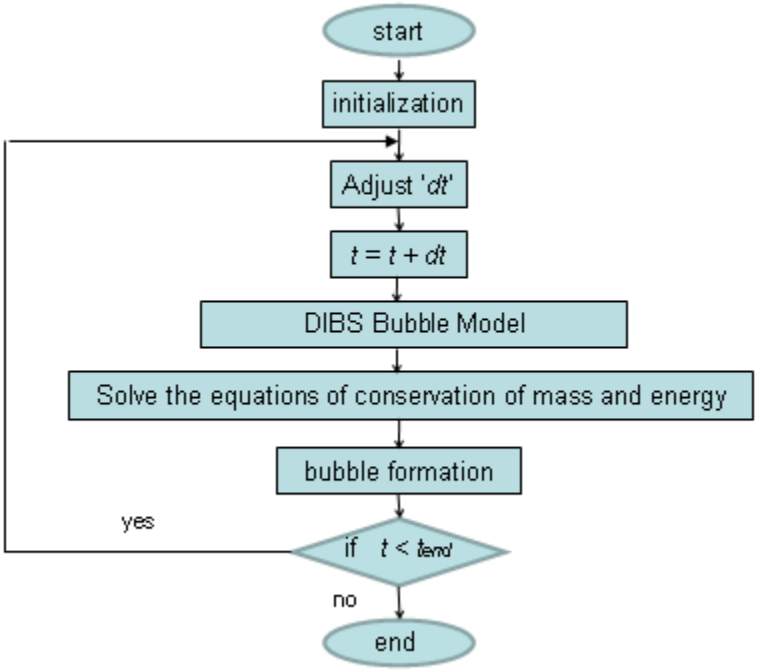

Figure 3.6: Flowchart of Gas-solid-bubble Simulation. A computational simulation for bubbling gas-solid fluidized bed uses DIBS model for tracing bubbles and uses Navier-Stokes equations and continuity equations for gas phase and particle phase.

regime, bed physical size and other experimental parameters in a fluidized bed as is depicted in two examples in Figure 2.2. For wall confinement, nonslip and free-slip boundary conditions are commonly used in many CFD approaches. A nonslip boundary condition means that the velocities are zero in all directions and are commonly used for gas flow. A free-slip boundary condition indicates that the velocity is zero in the normal direction with respect to the wall. For fine particles, Tsuo and Gidaspow [75] suggest that the boundary condition may be between free-slip condition and nonslip condition. In our study, we choose to approach the problem with a simplified one-dimensional case to study the global dynamical behavior of emulsion phase and bubble phase. In this case, no wall boundary condition needs to be considered for the emulsion phase, as we discuss the approach in the next section. A detailed discussion of the wall boundary conditions can be found in Tsuo and Gidapow's paper [75].

3.2.2 One-dimensional Discretization and Finite Difference Scheme

As described in previous chapters, the gas (or liquid) and particles phases are combined into a single emulsion phase when dealing with fine particles such as powders and catalysts in a fluidized bed. Thus in this case, there is only one set of two equations, an equation for mass balance and an equation for energy balance, for the emulsion phase as presented before. By adopting the DIBS model for bubble dynamics, the equation for energy conservation is intuitively replaced by the DIBS model and thus we only need one equation for conservation of mass, namely, the continuity equation

$$\frac{\partial V_f}{\partial t} + \frac{\partial}{\partial z}\left(V_f u_e\right) = 0, \tag{3.14}$$

where V_f is the volume fraction and u_e is the velocity of emulsion flow in the vertical or z direction.

To seek a numerical solution in this case, the fluidized bed can be divided into slices (or species) where each slice has its own value of velocity as illustrated in Figure 3.7. In reality, the emulsion phase often has circulation behavior in a fluidized bed. Each slice might have some areas with upward emulsion velocities and some areas with downward velocities. The goal of dividing the fluidized bed into such slices is to seek the average flow velocity for each slice.

By applying the finite difference method to the previously mentioned partial differential equation (3.14), the problem can be solved using the following scheme:

$$u_{i+1}^{n+1} = \frac{1}{V_{i+1}^{n+1}}\left[V_i^{n+1}u_i^{n+1} - \frac{\Delta z}{\Delta t}\left(V_i^{n+1} - V_i^{n}\right)\right], \tag{3.15}$$

where i refers to the i-th slice and n is the index for time steps.

There will be no wall boundary conditions to be considered in this case. The only

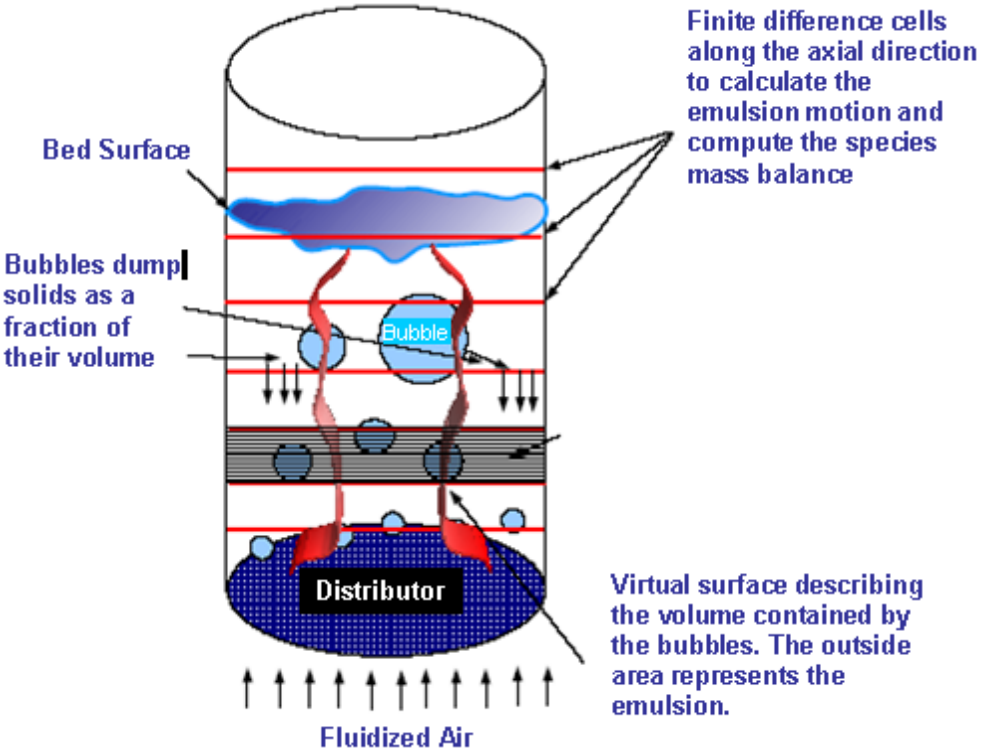

Figure 3.7: Numerical simulation of emulsion phase. By dividing the fluidized bed into slices, the numerical solution for emulsion phase can be reduced to a one-dimensional case.

initial condition of this particular one-dimensional case is that the emulsion velocity of the first slice is equal to the superficial velocity of the flowing medium (gas). Namely, $u_1^n = u_s$, at any time step n. For the time step $n+1$, the change of void fraction in each slice can be computed after bubbles are traced by the DIBS model. Thus the velocity for each slice can be obtained through Eq. (3.15). For each slice, the velocities of emulsion phase can be collected as a time series from the computational implementation and then can be further analyzed by time series methods.

Chapter 4

Bifurcation Analysis of Single-Bubble Injector

4.1 Motivation

The goal of the bifurcation analysis is to seek control guide for engineering fluidized beds through numerical simulations and data analysis on some identified key elements. To achieve this goal, some data analysis methods are needed to understand the expected nature of the dynamical information such as the generation and transmission of information and self-organization into spatio-temporal systems.

In the last decade, Skrzycke *et al.* [71], Daw *et al.* [19, 21], Daw and Halow [17, 18], and Schouten *et al.* [5, 67, 68] demonstrated in their research work the association of low-dimensional deterministic chaotic phenomena in the dynamics of bubbling fluidized beds. These results indicate the possibility of controlling the fluidization dynamical behavior through perturbation techniques on some sensitive parameters.

The DIBS bubble model can be viewed as a more general class of models referred to as self-propelled particle systems [9]. Using the DIBS model, Pannala *et al.* [58] studied the collective behavior of large numbers of rising bubbles and showed that the

DIBS model can produce so-called channeling behavior in which large-scale numbers of bubbles tend to collapse toward the center of the flow. The early works in studying the chaotic behavior of bubble dynamics within a fluidized bed are based on the data collected from actual experiments, mainly the time series from pressure signals via monitoring the pressure within fluidized beds. Therefore, it would be interesting to explore the computational approach with the DIBS model for bubble dynamics in more details, in particular the transitions among different chaotic regimes for some sensitive parameters, or bifurcation parameters.

Key issues involved in conducting bifurcation analysis of bubble dynamics within bubbling fluidized bed are:

1. What is the detailed nature of the local bifurcations generated by varying values of sensitive parameter(s)?

2. What is the effective dimensionality in the local dynamics compared with the original bubble model used?

3. What level of predictability should be expected based just on the local measurements?

The answers to the above questions will allow a better understanding of the expected nature of the dynamical information that should be available to a typical experimental observer. Although the focus of bifurcation analysis for questions (1), (2) and (3) is not directly on the issue of fluidized-bed control (as did Kaart *et al.* [39] and De Korte *et al.* [44]), they are obviously related to control. It will be exciting to see such study through computational modeling and numerical simulation produce results that are consistent with typical experimental observations and as well as with those early research works of last decade.

4.2 Bifurcation Parameter and Measurement Variable

In our DIBS computational simulations, bubbles are generated periodically from the bottom of the porous plate as described in Section 3.1.2. One of the main parameters is the bubble injection frequency (BIF). Therefore a straightforward idea would be to see the change of the bubble dynamics by varying the BIF values. A BIF value is used by the simulation program to form bubbles periodically and has, of course, practical significance in controlling fluidized bed performance. Notice that the BIF is not shown in Eq. (3.8) of the DIBS model. Therefore, it is difficult to perform a bifurcation study analytically by just working directly on a cluster of equations. Fortunately, computational simulations allow such work to be possible to unravel the chaotic behavior of bubble dynamics in a bubbling fluidized bed.

The simulated experimental measurement is a hypothetical laser device that detects passing bubbles and records time series for rising bubbles that pass through a fixed observation point for single injector case as is depicted in Figure 4.1. Nguyen *et al.* [53] and Tufaile and Sartorelli [76, 77] successfully used this type of measurement to study bubble-train dynamics. Notice that the actual formation of bubbles is related to the superficial velocity of flow medium and minimum fluidization velocity (U_{mf}). Therefore, reasonable BIF values for numerical simulations are initially chosen from near 0 Hz to 10 Hz. Here n Hz is defined to be n bubbles to be generated per second by the simulated bubble injector.

After the data, the time for bubbles passing the laser detector, is collected, the time intervals, Δt_i (as is depicted in Figure 4.1), between two consecutive data points are computed offline and form a time series. By eliminating the transients, a bifurcation diagram is constructed which shows complex bubble dynamical behavior with fixed

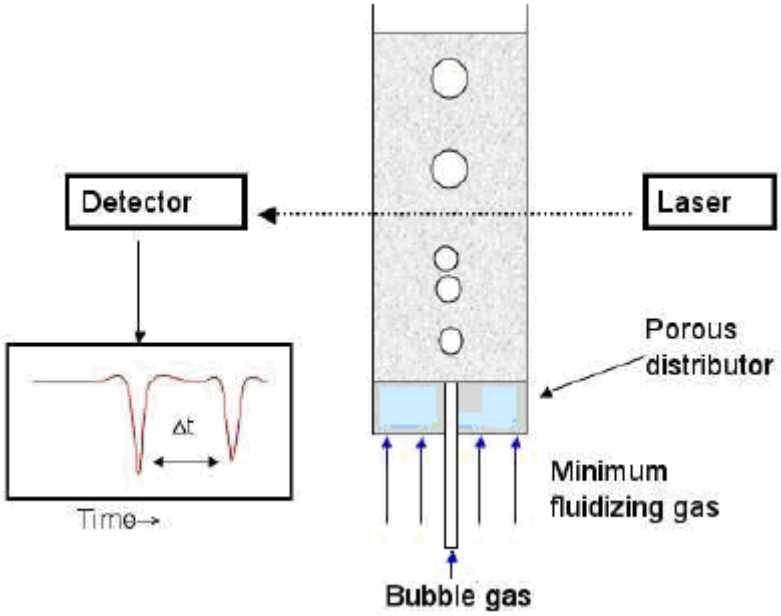

Figure 4.1: Experiment with Single Bubble Injector. A schematic diagram depicts the devices for detecting and recording the time of bubbles passing the observation point. The time interval between two passing bubbles, Δt, is calculated offline to form a time series to which the bifurcation analysis is carried for a single bubble injector case.

points, chaotic attractors, periodic solutions and intermittency behavior.

4.3 Computational Simulation

Based on the DIBS model described in Section 2.1, the movement of a bubble in a fluidized bed at each time step can be traced by solving Eq. (3.8) using typical numerical methods for ODEs. A computational code is programmed by integrating the ODE for all bubbles to trace their movements. We modified the software to include the algorithm allowing adjustable time step, dt, as mentioned in Section 3.1.2, with BIF values from a refined grid on (0, 10] to run computational simulations in parallel in cluster machines. In addition, the color scheme was implemented into the software to record bubble passage time. Table 4.1 lists the main values for the experiments

Initial bed height	40.0 cm
Bed diameter	22.9 cm
Bed Shape	Circular
U_{mf}	1.7 cm/s
Superficial Gas Velocity	1.7127 cm/s
Bubble injection frequencies	a 2000-point grid on (0, 10]
Initial bubble size	1.0 cm
Observation point	20.0 cm
Δt	0.001 s

Table 4.1: Main parameters for computational simulations of bubbling fluidized beds using DIBS model

carried out for bifurcation analysis.

To capture the long term behavior, the program runs for a minimum of 700 seconds and in some cases it runs up to 2400 seconds. The computationally intensive jobs demand use of high performance computing. The TeraGrid machine, a cluster with 102 teraflops computing capacity at the San Diego Supercomputer, was chosen to run all simulations. Four compute nodes, IA-64 1.5 GHz per node, were used to run simulations in parallel. Since each simulation (for a given BIF value) is an independent task, batch jobs of DIBS simulation for BIF values from a 2000-point grid on (0, 10] were launched by a Perl script, which is submitted four times into four compute nodes. Each Perl process runs the bubble simulation program for a subset of BIF values. In order to obtain a more detailed bifurcation diagram for BIF values inside [4, 6], simulations were carried out for a 2000-point grid on [4, 6] to create a zoomed-in picture of bifurcation diagram. The computation time, for instance, for the 2000-grid on the zoomed-in frequency interval [4, 6] is, approximately, 2.5 hours in each TeraGird node.

An initial real-time visualization was developed using native graphic functions and is very helpful for debugging the computer code and for verifying the correctness of the

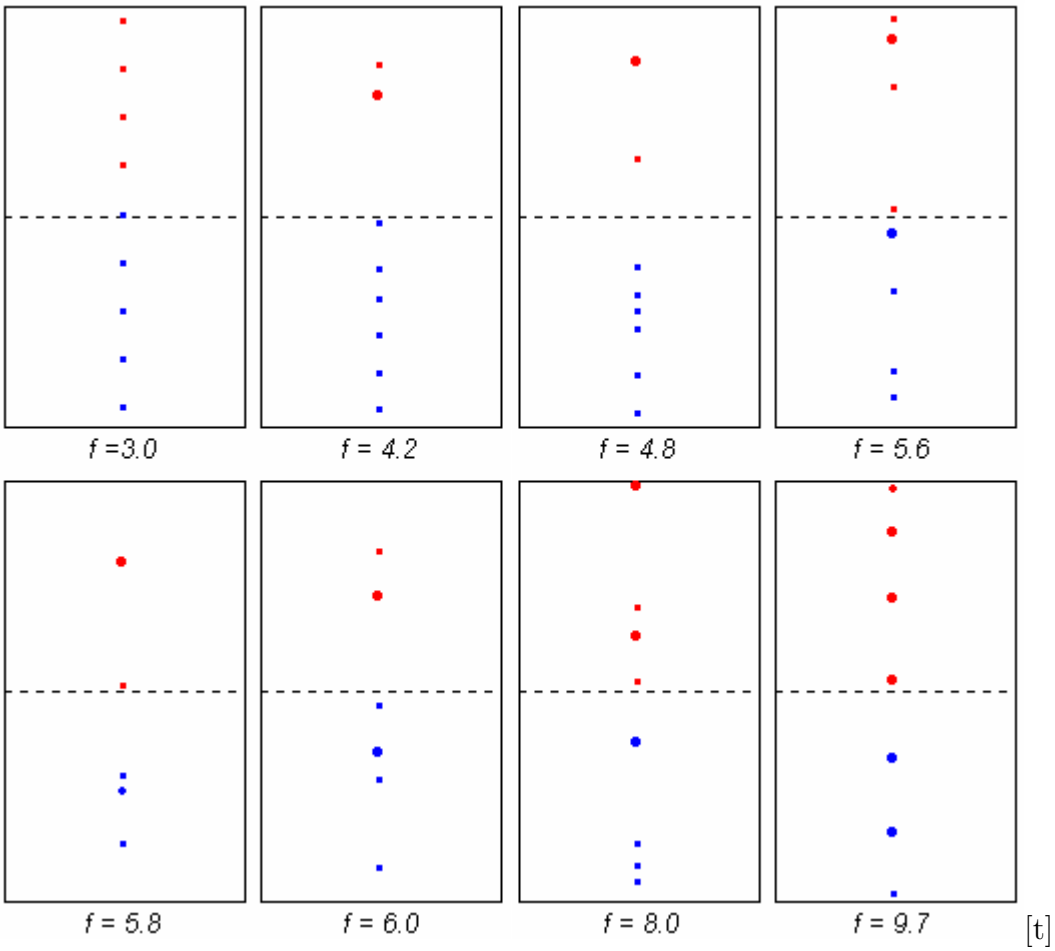

Figure 4.2: Single bubble injector simulations with various bubble injection frequencies. The bubbles below the observation line (laser detector) are colored in blue and bubbles passing the observation line are painted in red. The bed size is 20cm $\times$ 40 cm. The initial diameter of a bubble being injected from nozzle is 1 cm. The observation point is right in the middle height of the bed.

implementation. This first version of the bubble visualization software was initially developed in two-dimensions and displays rich visual information showing bubble movement (rising upward rapidly) and bubble coalescence. Figure 4.2 shows some snapshots of numerical experiments with different BIF values. A more sophisticated three-dimensional visualization display was developed later in studying the bubble dynamics with multiple bubble injectors and will be shown in the next chapter.

Experiments with observation points at other two locations, $h = 10$ cm and $h = 30$

cm are also carried out in this study. The resulting bifurcation diagrams with these two observations points demonstrate similar dynamical behavior with great tendency towards orbits of higher period as the observation point decreases. The time series analysis work in this research work mainly concentrates on BIF values in Figure 4.2.

4.4 Bifurcation Analysis for Single-Nozzle Injector

In this work, a single bubble nozzle injector case, centered in the bottom of a fluidized bed, is considered to investigate the underlying bifurcations of bubble dynamics from DIBS model. A bifurcation diagram is constructed by varying the bubble injection frequency (f). The computationally based bifurcation analysis shows that the bubble dynamics transits among different regimes such as fixed point, chaotic attractors and intermittent behavior. Using time series analysis methods, the embedding trajectories in phase space with selected embedding dimension shows attractors, etc. and allow linear fitting to be carried successfully for long term prediction. The maximum Lyapunov exponents, approximated computationally for a wide range of injection values, indicates clearly the chaotic behavior of bubble dynamics.

4.4.1 Bifurcation Diagram

The purpose of constructing a bifurcation diagram is to unravel the long term behavior of a given dynamical system and transitions among different dynamical regimes for identified bifurcation parameter(s). The BIF values, chosen from a fine grid of 2000 points, evenly distributed on $(0, 10]$, are used for constructing a bifurcation diagram. For each BIF value, the DIBS simulation runs for 700 seconds to record the time series, $\{t_i\}$, bubble passage time through a laser detector. The actual signals, $\{\Delta t_i\}$, the time interval between two consecutive data points, are calculated offline. The

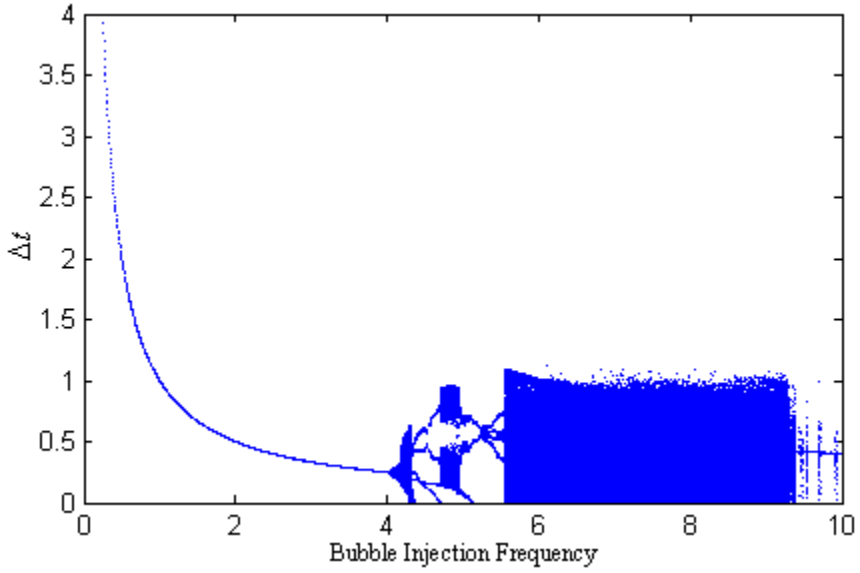

Figure 4.3: The bifurcation diagram of bubble dynamics with the experimental configurations described in Section 4.3. As bubble injection frequency (BIF) is small, the global dynamics is attracted to a fixed point. As BIF value goes beyond 4.0 to 10.0, the global dynamics changes to chaotic region, period-4 oscillation, four chaotic attractors, periodic oscillation, a region with intermittent behavior, and then into a region with nearly a fixed point.

first 200 points of computed $\{\Delta t_i\}$ are treated as transients and are discarded. A bifurcation diagram is constructed by plotting the resulting time series against the BIF values. This computational method has been widely used for constructing bifurcation diagrams. One typical example is the bifurcation diagram for logistic equation by Alligood *et al.* [2]. Figure 4.3 and Figure 4.4(a) are the bifurcation diagrams from the DIBS simulations for the configurations described in Section 4.3.

At low injection frequencies, bubbles in the fluidized beds are significantly separated and the bubble-bubble interactions have very little impact on rising bubbles. Thus bubbles rise as a stream with almost fixed gap between two consecutive bubbles. This results in a fixed value in $\{\Delta t_i\}$. This demonstrates that the global dynamics is attracted to a fixed point for low BIF values. As the BIF value increases beyond $f = 4$ Hz, bubbles start to coalesce and the global dynamics rapidly changes from

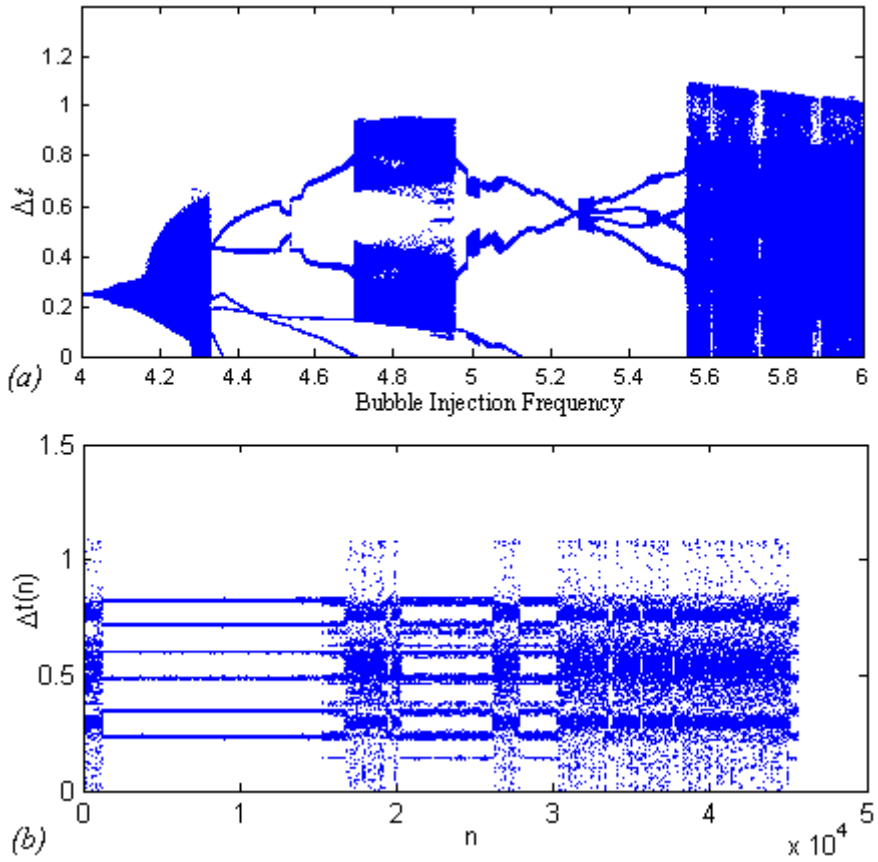

Figure 4.4: (a) A zoomed-in bifurcation diagram for BIF values in the range [4, 6] Hz. The diagram demonstrates clearly the transition from a single chaotic attractor, to period-4 oscillation, to four chaotic attractors, to period-3, to period-2, to period-4 oscillation and finally to intermittent chaotic region. (b) The time series plot for BIF at $f = 5.6$ Hz. The dynamics demonstrates intermittent behaviors between period-6 oscillations and chaotic regions. The plot is constructed by running the DIBS simulation for 2400 seconds.

a fixed point to a region of quasi-periodic behavior that eventually becomes chaotic. The global dynamics enters a more organized region of period-4 oscillation for 4.3 Hz $< f <$ 4.7 Hz, roughly. After this region, the period-4 region bifurcates into a chaotic region with four attractors (see Figure 4.4(a)). Near $f = 5$ Hz, the dynamics again enters a region with period-3 oscillation that changes into a period-2 orbit. The period-doubling bifurcation then leads to a period-4 orbit.

Beyond $f = 5.5$ Hz, the system displays intermittent behavior in which the under-

lying dynamics randomly change between a high period orbit, period-6 and a chaotic attractor. Figure 4.4(b) is the time series plot of $\{\Delta t_i\}$ from running the DIBS simulation for 2400 seconds for BIF value at $f = 5.6$ Hz, which corresponds to the thick area in Figure 4.3. From the time series plot, the bubble dynamics demonstrates clearly the intermittent behavior as the system transit among period-6 oscillations to chaotic regions. This suggests that there are certain flow conditions in which control may be extremely difficult.

4.4.2 Phase Space Embeddings

Phase space embedding is an important method in studying nonlinear time series. In a deterministic system, the state for all future times is determined once an initial state is given. Thus, the idea of phase space reconstruction is to use a one-to-one and continuous function, more precisely a topological mapping, to embed the one dimensional time series from a deterministic dynamical process into a multi-dimensional space to disclose the real manifold in which the dynamics takes place and to allow prediction for future evolution of the dynamical system. A typical technical solution is the method of delays. Assume $\{s_n\}$ is a given time series. New vectors are formed by defining the delay coordinates as:

$$\vec{s} = \left(s_{n-(d-1)\tau}, s_{n-(d-2)\tau}, ..., s_n\right), \tag{4.1}$$

where d is called the embedding dimension and τ is delay or lag.

The embedding theorems established by Takens [72] in 1981 and Sauer *et al.* [65] in 1991 guarantee the existence of such d (when d is sufficient large) so that the time delay embedding produces a true embedding from original time series to the space R^d.

The embedding dimension d reveals that there are d independent measurements

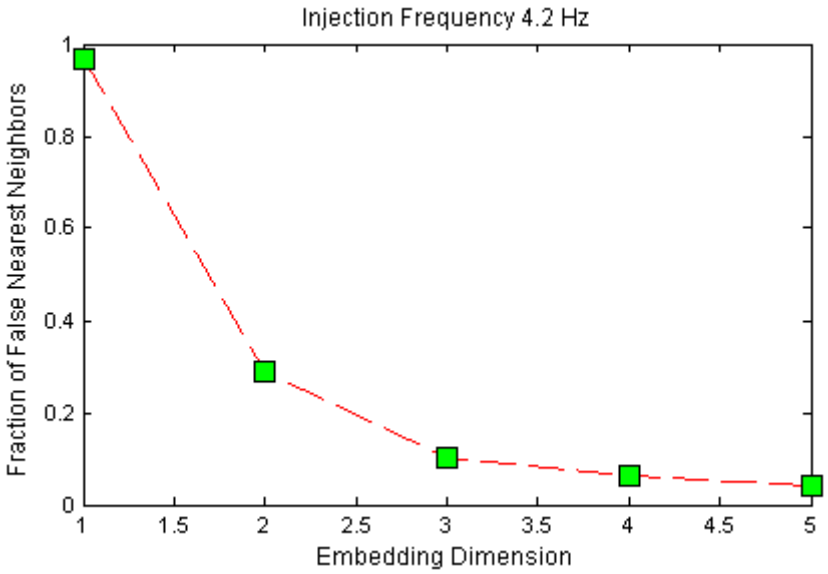

Figure 4.5: A plot for the results using false nearest neighbor (FNN) method implemented in TISEAN software for the time series at $f = 4.2$. The plot shows that a good estimate for the embedding dimension is $d = 3$. This is because there is a significant drop in the percentage of false nearest neighbors when d changes from 2 to 3. The embedding dimension $d = 3$ is empirically determined from this graph.

within a given time series. It is then natural to ask how to find the minimum embedding dimension as the existence of such numbers is guaranteed. The computational method adopted by this study to find the minimum embedding dimension is the false nearest neighbor (FNN) method originally proposed by Kennel *et al.* [43] and was implemented by Hegger *et al.* [38, 41] in their TISEAN software package. The FNN method is based on the idea that neighboring points of a given point are also mapped to neighbors in delay space by a true embedding. For a delay map with embedding dimension $d < d_{min}$, such topological properties would no longer be preserved and would produce false neighbors after mapping into the delay space.

In the DIBS model, the local dynamics of a single bubble injector will be dominated by pairwise interactions between leading and trailing bubbles. The bubble stream also tends to collapse toward the bed center as the bubbles rise. This should tend to reduce the effective local dynamical dimension considerably. Based on these

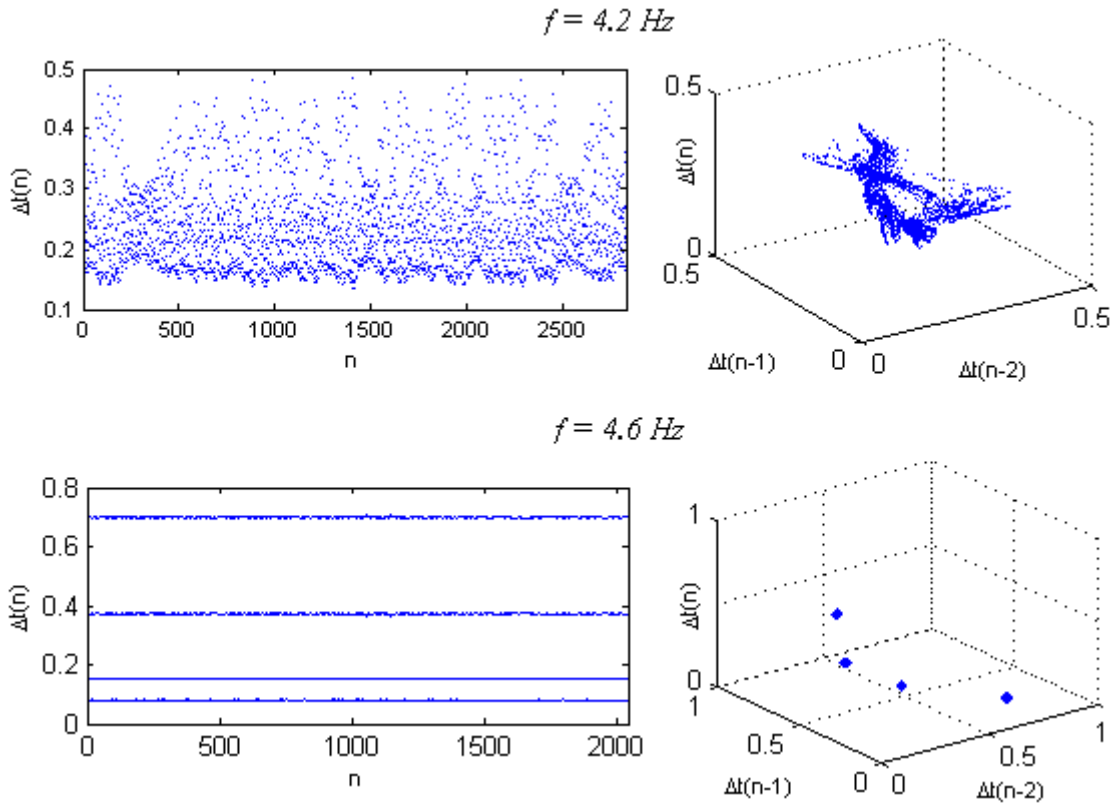

Figure 4.6: Time series plots and their corresponding phase portraits for the data from DIBS simulations. Two pictures on left side are the time series plots for $f = 4.2$ and $f = 4.6$. The pictures on the right side are the phase portraits using embedding dimension $d = 3$.

facts, it is reasonable to expect the crossing dynamics to be described by a map of the form $\Delta t_{n+1} = G(\Delta t_n, \Delta t_{n-1})$ for the time series from the DIBS simulation. Namely, the anticipated embedding dimension required to resolve the local dynamics to be close to a value of $d = 3$. Figure 4.5 shows the resulting plots after applying FNN algorithm from TISEAN package for the time series from the DIBS simulation with BIF value at $f = 4.2$ Hz. Notice there is less than 0.1 change of the false nearest neighbors when d changes from 3 to 4. It is then reasonable to assume that the required embedding dimension is $d = 3$. This result matches the expected embedding dimension. Other results show the embedding dimensions to be $d = 3$ for various BIF values.

Proceeding with an assumed dimension of $d = 3$, the time delay map for the DIBS model can be written as: $\Delta T_n = (\Delta t_n, \Delta t_{n-1}, \Delta t_{n-2})$. Figure 4.6 shows two time series plots and their phase space embedding portraits for two BIF values, $f = 4.2$ Hz and $f = 4.6$ Hz. The phase portrait for $f = 4.2$ shows an attractor after the time series of bubble passge time is embedded into phase space.

4.4.3 Model Fitting

With the embedding dimension determined to be $d = 3$, the embedding function of the time series to phase space becomes $\Delta T_n = (\Delta t_n, \Delta t_{n-1}, \Delta t_{n-2})$. With the new embedded points on the trajectory in phase space, a typical question would be to find a map, at least computationally, to model the deterministic evolution of the new time series $\{\Delta T_n\}$, namely, we seek a nonlinear map of the form: $\Delta T_{n+1} = F(\Delta T_n)$, for the purpose of forecasting future trajectory in phase space, eventually for original time series, as is depicted in Figure 4.7. Many nonlinear prediction models for time series have been studied since early 1990s. Well-studied models are global polynomial model fitting and local linear model fitting. The resulting fitting map then can be used computationally to forecast the future trajectory and to evaluate the Lyapunov exponent spectrum.

The local linear model was introduced by Eckmann *et al.* [23] in 1986 and Farmer *et al.* [26] in 1987. This model is first chosen to do the fitting for the time series of the bubble dynamics. With the embedding vector as $\Delta T_n = (\Delta t_n, \Delta t_{n-1}, \Delta t_{n-2})$, both T_n and T_{n+1} have the same Δt_n and Δt_{n-1}. Thus it suffices to find a map f for the last component such that $\Delta t_{n+1} = f(\Delta T_n)$. The simplified case leads to approximate f by a linear function of the form $f(\Delta T_n) = \vec{a}_n \cdot \Delta T_n + b_n$. The vector $\vec{a}_n$ and the

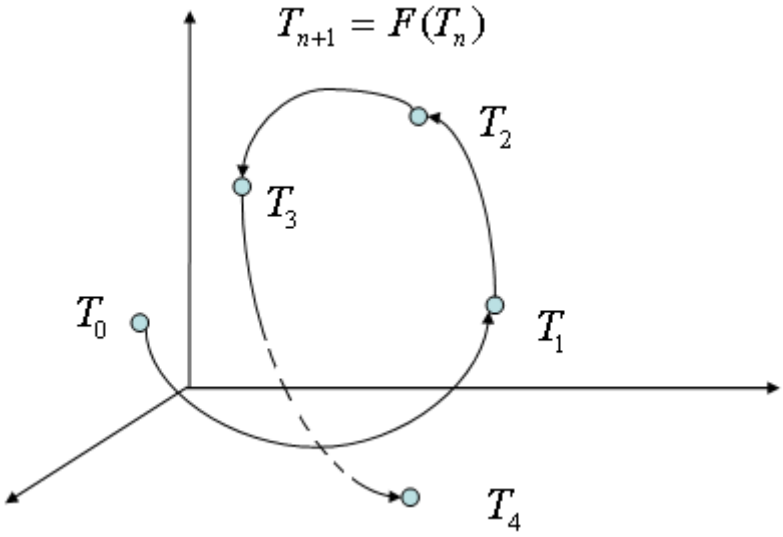

Figure 4.7: Model Fitting for Dynamical System. The phase space map, F, is the fitting nonlinear map based on embedded points from a given time series. The map can be used to forecast future trajectory and to compute the Lyapunov spectrum.

scalar b_n are then found by minimizing:

$$\sum_{i=1}^{M} \|\Delta t_{n+1} - \vec{a}_n \cdot \Delta T_i - b_i\| \tag{4.2}$$

where M is the total number of time delay vectors.

The TISEAN software provides two routines, *onestep* and *nstep*, that implement the local linear fitting algorithm for a given time series. The *onestep* takes input of time series data and outputs the forecasted error with the local linear fitting model. The important arguments in using the routine are the embedding dimension, delay, and neighborhood size. The routine, *nstep*, uses the same inputs as those for *onestep* and it produces the predicted trajectory by applying the fitting algorithm with the given time series data. Detailed information of the TISEAN software can be found in the online manual by Hegger *et al.* [37].

For the time series of bubble dynamics generated by DIBS simulations, the local linear fitting works very well for a wide range of BIF values up to $f = 5.55$ Hz. Figure

4.8 shows the predicted trajectories (in black) of 2000 iterations and the input time series from DIBS simulation (in green) at two representative BIF values at 4.2 Hz and 4.8 Hz. The relative forecast errors, defined to be the normalized errors to the variance of the data, for $f = 4.2$ Hz and $f = 4.8$ Hz are 0.215 and 0.068, respectively.

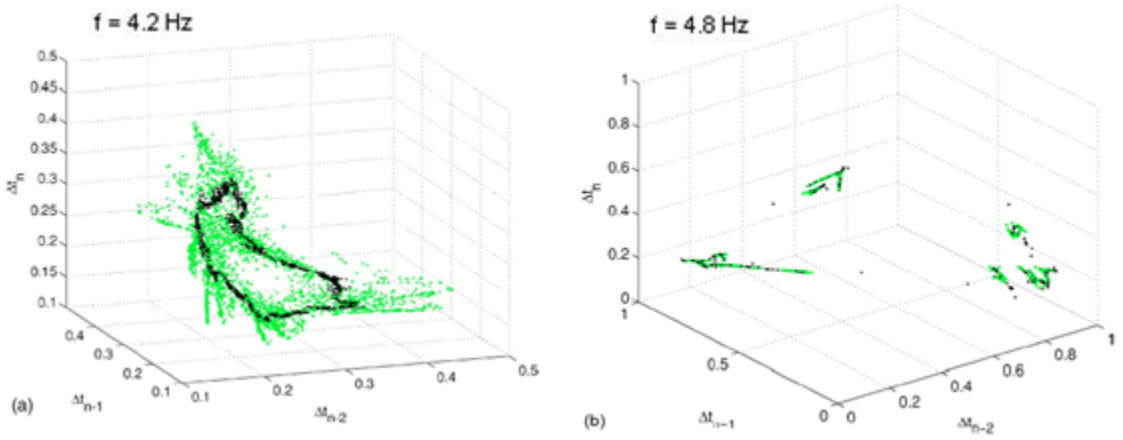

Figure 4.8: Using data fitting technique, a map F can be constructed to forecast future trajectory and to compute the Lyapunov spectrum. The black dots in the graphs are original time series formed by bubble passage time. The black dots are the predicted data generated by the local linear prediction method.

Beyond $f = 5.55$ Hz, where the system exhibits intermittency between periodic orbits and chaotic attractors, both approximation methods, local linear fitting and global nonlinear multivariate polynomial fitting, failed to produce adequate long-term predictions.

4.4.4 Lyapunov Exponent

Lyapunov exponents indicate the future growth and decay rate for a small initial perturbation as is depicted in Figure 4.9. It is a quantitative measure for the sensitivity of a dynamical system on initial conditions. It is also an important indicator for a dynamical system to have a potentially chaotic behavior.

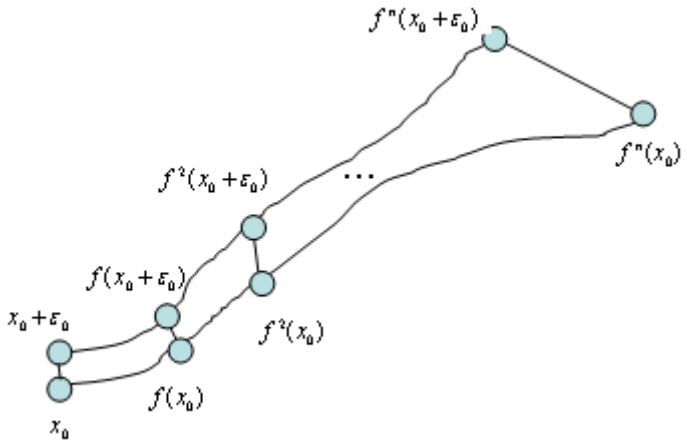

Figure 4.9: Small Perturbation and Lyapunov Exponent. The value of Lyapunov Exponent indicates future growth or shrinkage rate for a small perturbation in a dynamical system. It is also an indicator for a dynamical system to have chaotic behavior.

For a one-dimensional discrete map, $x_{n+1} = F(x_n)$ and a given initial state x_0, the maximum Lyapunov exponent is defined to be the logarithmic value of the divergence between two trajectories separated by a small perturbation ε_0 :

$$\lambda = \lim_{n\to\infty} \lambda(n) = \lim_{n\to\infty} \frac{1}{n} \ln \left(\frac{\|f^n(x_0+\varepsilon_0) - f^n(x_0)\|}{\|\varepsilon_0\|} \right). \tag{4.3}$$

By computing the maximum Lyapunov exponents for the time series from DIBS simulations, $\{\Delta T_n\}$, the rates, at which neighboring orbits on each individual attractor diverge (or converge), can be quantified as the time-passage dynamics evolves in time.

Many computational algorithms have been proposed for computing an estimate of the maximum Lyapunov exponent. The TISEAN software package implements two main algorithms for computing the maximum Lyapunov exponent. One is the algorithm by Rosensetein *et al.* [64] and by Kantz [40], which tests directly the exponential divergence of nearby trajectories. Another algorithm is to compute the Lyapunov spectrum by estimating the local *Jacobians* from a fitting model in em-

bedding space. Unfortunately none of these works with the time series from DIBS simulations when BIF values are very small. This is obviously because the software quickly encounters singularities when computing on a series of fixed numbers.

Notice that the above algorithms target finding a numerical estimate of the maximum Lyapunov exponent for a given time series. With the DIBS simulation, we finally chose a simpler approach: a small perturbation can be achieved by delaying one bubble with a small time δt by moving the bubble with a small distance in the vertical direction at some time t_1 in the DIBS simulation. It is crucial that the time series from the perturbed DIBS simulation is created from the same dynamical system. If two bubbles that do not coalesce in original system below the observation point, for example, merge after perturbation, the original time series and the perturbed time series are created actually from two different dynamical systems. To avoid such problem, we developed a perturbation scheme in which the computational program keeps looking for a pair of neighboring bubbles under the observation point that have fairly large gap between them, e.g., 1 cm (the bed height is 40 cm). Once the program finds such pair of bubbles, the top bubble is perturbed with a small distance that is much smaller than 1 cm.

An estimate of the maximum Lyapunov exponent is computed by averaging $\lambda(n)$ in Eq. (4.3), for the purpose of obtaining a more statistically meaningful measure of the maximum Lyapunov exponent, with the formula:

$$\lambda = \frac{1}{N} \sum_{i=1}^{N} \lambda(i). \tag{4.4}$$

In practice, a small perturbation of $\delta t = 0.05$ generates very good results of maximum Lyapunov exponents for a wide range of injection frequencies as is shown in Figure 4.10. Observe that the sign of the exponent agrees with the attractor depicted by the bifurcation diagram. That is, for low frequencies, the largest exponent

is negative, indicating convergence towards the fixed point, as is normally observed in laboratory experiments as well as in the DIBS simulations. A positive Lyapunov exponent along with the fact that $\{\Delta t_n\}$ has an upper bound (which will be explained next) is indicative of deterministic chaotic behavior in the passage-time dynamics.

Another important fact is the existence of an upper bound for the time series $\{\Delta t_n\}$. From formula (3.8) for the velocity of a rising bubble, we can see that the velocity term has a lower bound, denoted as $\|v\|_{min}$, that is attained once the experimental parameters, such as bed size and initial bubble diameter, are fixed. Thus the upper bound for crossing time, namely for the time series $\{\Delta t_n\}$ is:

$$\Delta t_i \leq \frac{H_{max}}{\|v\|_{min}} + \frac{1}{f}, \tag{4.5}$$

where H_{max} is the maximum height of the bed and f is the bubble injection frequency.

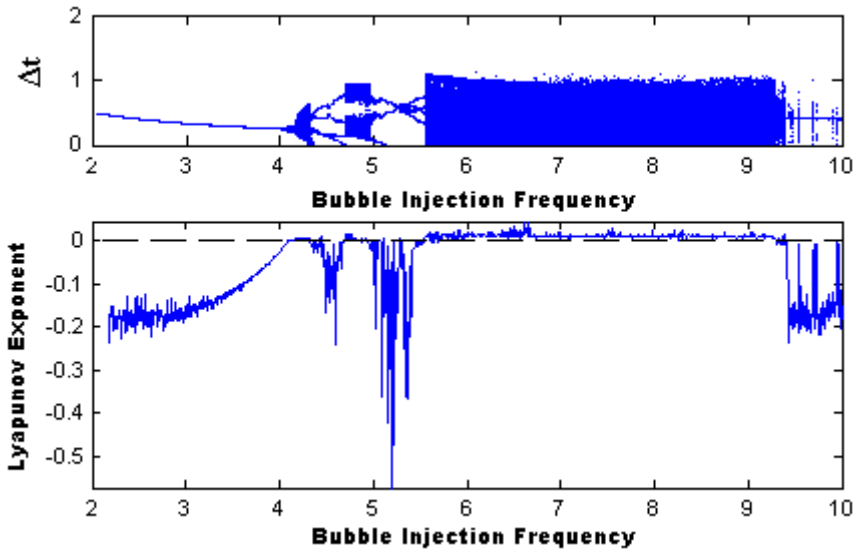

Figure 4.10: Computational results of maximum Lyapunov exponents of bubble dynamics for various values of injection frequencies. A positive exponent is indicative of chaotic behavior in the system's dynamics. Fixed points in time series match well with negative Lyapunov exponents.

For frequencies larger than $f = 5.55$ Hz, the sign of the largest exponent is mainly positive. In this region, however, the time-passing dynamics is not only chaotic but

rather intermittent, randomly switching between chaotic attractors and high-period orbits. Observe also that the maximum Lyapunov exponent is zero at the points of bifurcation where the system dynamics changes behavior.

The presence of intermittency in the bifurcation sequence is likely to be difficult to observe experimentally because of the presence of parametric noise, *e.g.* from gas-flow turbulence or granular particle flow. Such noise would be expected to continually stimulate intermittent jumps in these areas of the bifurcation sequence, thus causing the periodic features to be blurred into an apparent broad band of chaos.

Chapter 5

Spatio-Temporal Analysis of Fluidized Beds

With multiple bubble injectors, the bubble dynamics becomes more complicated. Bubble coalescence not only happens in the vertical direction but it also occurs in various directions. As bubble injection frequency increases, a large number of bubbles are present in the fluidized bed, moving upward and coalescing with each other. To capture the bubble dynamics with multiple injectors, the bubble dynamical process is digitized into frames to construct a data matrix. By applying the proper orthogonal decomposition method, spatial and temporal information are decoupled. Energy plots can be constructed to review the dominant modes for the dynamical system, while time series analysis techniques can be applied to study the temporal behavior captured by the time-dependent coefficients associated with the spatial modes.

5.1 Proper Orthogonal Decomposition

The Proper Orthogonal Decomposition (POD) has been widely used for data analysis in fluid dynamics, identification and control in chemical engineering, oceanography, image processing, and biomedical engineering. By determining an optimal basis for

the reconstruction of a given data set, the POD is a technique used to reduce a multidimensional dataset to lower dimensions. The POD is also known as principal components analysis (PCA), Karhunen-Loéve decomposition, and singular value decomposition [42, 48, 61]. By applying the technique for the digitized bubble dynamics, the POD creates spatial and temporal decompositions for the given multi-dimensional input. This allows us to carry time series analysis for the resulting time series of temporal evolution data and apply the appropriate prediction model. To understand this, a brief review of the theoretical aspects of the POD analysis is necessary.

A multi-dimensional time series data can be viewed as data points from scalar functions $u(x, t_i), i = 1, 2, ...M$. These functions are assumed to form a linear infinite-dimensional Hilbert space L^2 on a domain D, a bounded subset in R^n, and are parameterized by t_i, which represents time.

The POD extracts time-independent orthogonal basis functions, $\Phi_k(x)$, and time-dependent orthogonal amplitude coefficients, $a_k(t_i)$, such that the reconstruction of the data points

$$\vec{u}(x, t_i) = \sum_{k=1}^{M} a_k(t_i)\vec{\Phi}_k(x), \quad i = 1, 2, ..., M, \tag{5.1}$$

is optimal for the least square fit for

$$\left\langle \left\| \vec{u}(x, t_i) - \sum_{k=1}^{m} a_k(t_i)\vec{\Phi}_k(x) \right\|^2 \right\rangle, \tag{5.2}$$

for any given number $m \leq M$ over any subsets of orthogonal basis. Here $\|\cdot\|$ represents the L^2-norm. The $\langle\cdot\rangle$ is the time average for a given sequence from scalar functions by:

$$\langle \vec{u}(x, t_i) \rangle = \frac{1}{M} \sum_{i=1}^{M} \vec{u}(x, t_i). \tag{5.3}$$

The functions $\{\Phi_k(x)\}$ are called empirical eigenfunctions or POD modes and are the

eigenvectors for the tensor product matrix:

$$R = \frac{1}{M}\sum_{i=1}^{M} \vec{u_i}\vec{u_i}', \tag{5.4}$$

i.e.

$$R\vec{\Phi}_k = \lambda_k \vec{\Phi}_k. \tag{5.5}$$

The important fact about this decomposition is that it generates spatial and temporal decompositions $\{\vec{\Phi}_k\}$ and $\{a_1(t_i), a_2(t_i), ..., a_M(t_i)\}$. Thus for each k, $a_k(t_i)$ forms a single time series as t_i evolutes in time. This allows us to have spatial and temporal decompositions for a given multi-dimensional time series and carry time series analysis.

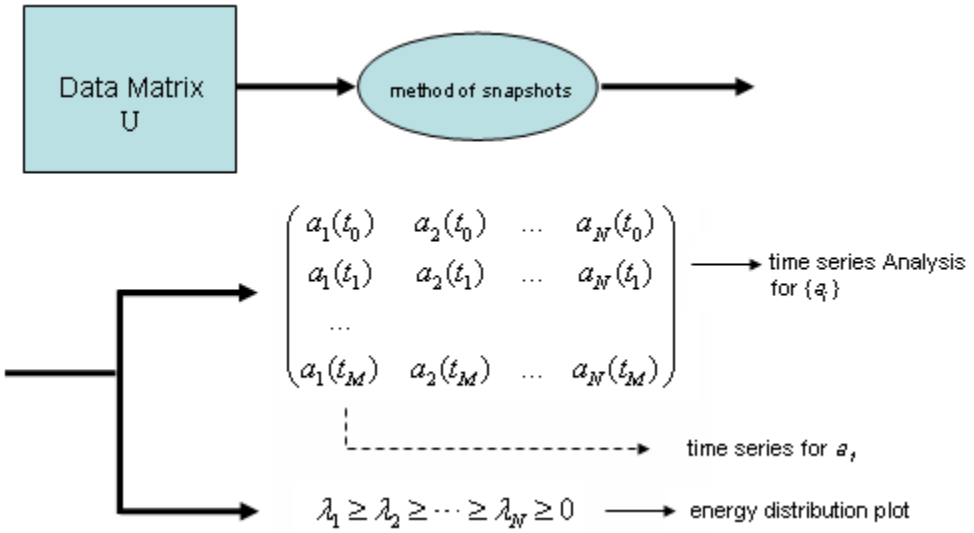

Figure 5.1: The procedure of the Proper Orthogonal Decomposition(POD). The data matrix is formed by aligning each frame data into one column in the data matrix U. $\{\lambda_1, \lambda_2, ..., \lambda_N\}$ are eigenvalues from the symmetric matrix $(1/M)U'U$ and are the results from the method of snapshots along with the matrix $(a_i(t_k))$.

A computational method, known as the *method of snapshots*, was developed by Sirovich [70] in 1987 for computing the spatial and temporal decompositions for a given data set from observations. It is based on the fact that both original data

vectors $\{u_k\}$ and eigenfunctions $\{\vec{\Phi}_k\}$ span the same vector space. Therefore, we can write

$$\vec{\Phi}_k = \sum_{i=1}^{M} v_i^k \vec{u}_i, \quad k = 1, 2, ..., M \quad . \tag{5.6}$$

Combining Eqs. (5.3) and (5.4), the coefficients v_i^k can be obtained by calculating the eigenvectors of the eigenvalue problem: $Cv = \lambda v$, where C is the symmetric matrix defined by $c_{ij} = (1/M)(\vec{u_i}, \vec{u_j})$, with $(\vec{u_i}, \vec{u_j})$ being the inner product of two vectors in a Euclidean space. Therefore, the eigenvectors of the $N \times N$ matrix R can be obtained by computing the eigenvectors of the $M \times M$ matrix C. Figure 5.1 depicts the procedure of applying the method of snapshots to obtain the spatial and temporal decomposition from an input matrix, which is made up of the experimental data from running bubble simulations with multiple injectors.

The eigenvectors of the matrix C can be computed by using the iterative QR method. The method of snapshot guarantees that non-negative eigenvalues, $\{\lambda_k\}$, of C are ordered in the decreasing order. In physical science, each λ_k represents the amount of energy for the corresponding mode, $\Phi_k(x)$. Thus the contribution of each mode for the dynamical system can be measured by its eigenvalue. The ideal case in doing POD analysis is that a few leading modes control 80% of total energy of the whole dynamical system. The total energy for a given experimental data set after POD decomposition is defined as the sum of all eigenvalues,

$$E = \sum_{k=1}^{M} \lambda_k. \tag{5.7}$$

The contribution of one particular mode to a dynamical system can be quantified as $E_k = \lambda_k / E$. Thus $\sum_{k=1}^{K} \lambda_k / E$ is the measure for the contributions of K leading modes.

5.2 Digitization of Bubble Dynamics

In order to apply the POD analysis, the bubble dynamics must be digitized to produce multi-dimensional time series by recording the images obtained from computer simulations. The digitization process will mimic one of the popular methods in studying fluidized beds via imaging system, in which the interaction between solids and fluids is continuously tracked. To digitize the bubble dynamics with multiple bubble injectors, rising bubbles are traced based on their projections onto a two-dimensional plane. A similar method is also used in studying spouting fluidized beds in which the actual fluidization process was recorded by video camera with lights in the other end of the fluidized bed at Oak Ridge National Laboratory. With the computer simulations, the projection of bubbles onto a two-dimensional plane can be easily traced numerically from the bubble data, including bubble positions and sizes. The computer program periodically produces one frame of data for bubbles inside the simulated fluidized bed and saves the information into a data file.

To generate one frame of data, a grid with pre-determined size is set on the projected rectangular area. For each block inside the grid, the area covered by the projected bubbles is computed. Then the fraction of covered area versus the area of the block is evaluated and is saved as the value for the block, or one component for the output vector of final multi-dimensional time series. Figure 5.2 demonstrates the procedure to compute one frame of digitized data for bubble dynamics inside a fluidized bed. When a fine grid is set to digitize the dynamical information, each small block can be viewed as a pixel in the whole image. Each block value comprises one cell value in the matrix for a digitized video frame. Then the data in the matrix is aligned into one column for the POD analysis.

Computing power must be considered in choosing the grid size. Although a finer

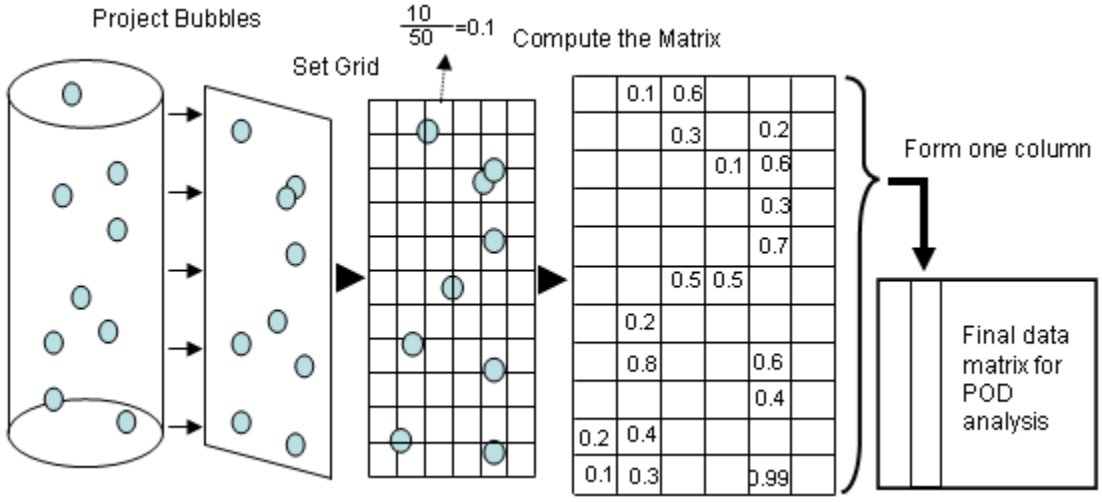

Figure 5.2: A schematic diagram for constructing one frame of digitized data for bubble dynamics. Rising bubbles are projected onto a plane. A grid is set on the rectangle area and the data in each block of the grid is computed based on the area covered by bubbles. A frame of digitized data is created and is aligned to form one column in the final matrix for POD analysis.

grid may create more accurate digitized information, the resulting data matrix can easily have the size beyond the computing capability of current computers. In the case of a 22×70 grid, 3520 frames were collected from bubble simulation, yielding a final data matrix of size 1540×3520.

5.3 POD Analysis of Bubble Dynamics with Multiple Injectors

In the DIBS simulation, multiple injectors are evenly distributed in the bottom plate. There are two options for generating bubbles. In the first option, all bubble injectors create new bubbles simultaneously. In the second option, bubbles are generated from randomly selected injectors. This is implemented by generating a random number of 0 or 1 for each injector to determine if a bubble needs to be formed. Since we are mainly interested in deterministic dynamical systems, the first option is selected for

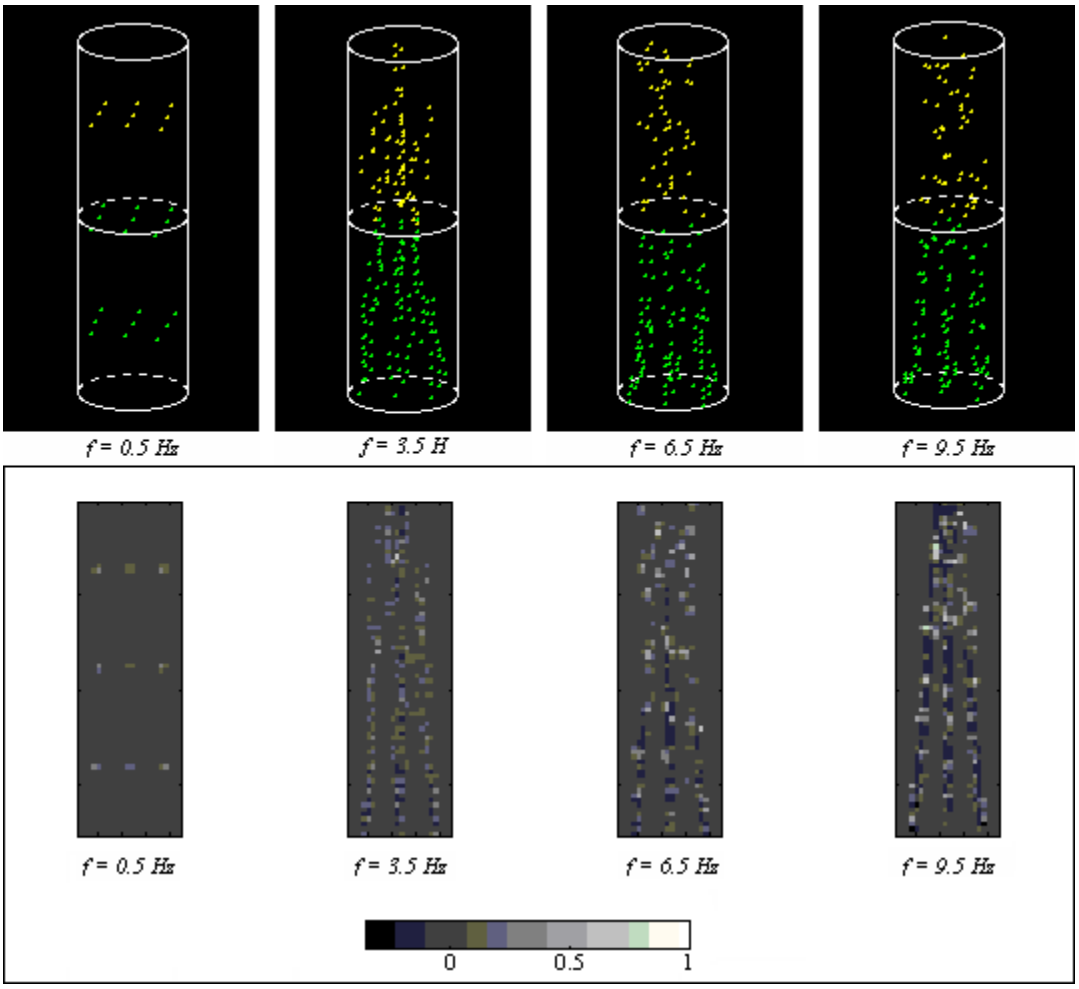

Figure 5.3: DIBS simulations with nine bubble injectors and their digitized frames. The images on the top are snapshots taken from the 3D real-time visualization for bubble simulation with multiple injectors. The images in the bottom are their corresponding images of digitized frames. The values in the matrix of a digitized frame are normalized.

our study and we leave the second bubble injection mode for future work.

Numerical experiments are first conducted with nine injectors that are sparsely distributed on the bottom plate with simultaneous bubble injection mode. The motivation is based on intuition that the behavior of the bubble dynamics should have similar patterns as those observed in a single bubble injector case since nine injectors are sparsely distributed. Several data points are picked from (0, 10] for BIF values

to conduct our research. A 3D visualization for the DIBS simulation is developed to monitor bubble dynamics in real-time. The top four images in Figure 5.3 show a group of snapshots from simulations with the BIF values taken at $f = 0.5$, $f = 3.5$, $f = 6.5$ and $f = 9.5$ Hz. Four pictures in the bottom of Figure 5.3 are the snapshots for the digitized frames with the chosen BIF values.

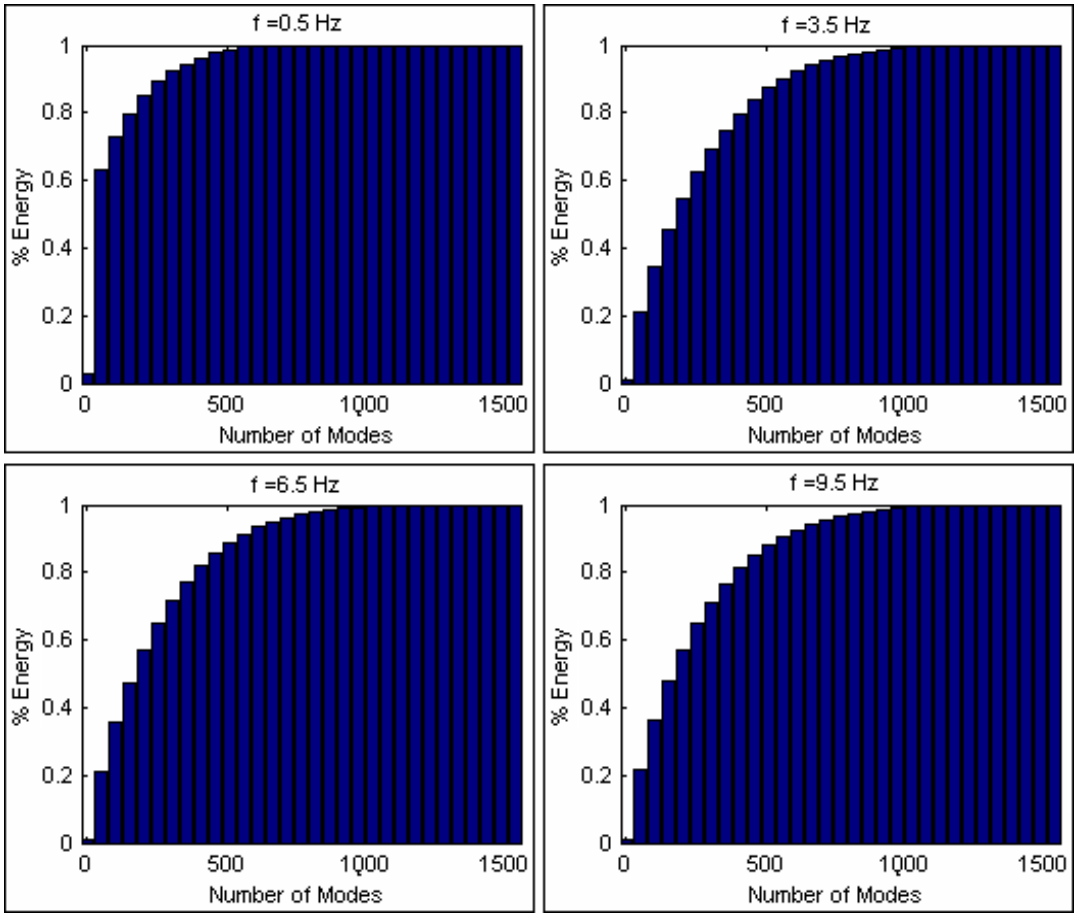

Figure 5.4: The energy distribution plots for four bubble injection frequencies after POD decomposition. The pictures demonstrate that usually it needs first $200 - 400$ modes to gain the 80% of the total energy.

Nine bubbles are generated simultaneously and move upward in parallel and form a layer of bubbles in the testbed. With small BIF value, there is a large distance between two layers of bubbles and thus there is no interaction or bubble coalescence

among bubbles. As the BIF value passes over a threshold around 1.0 Hz, bubbles start to interact with each other and coalesce. One common phenomenon with large BIF values is the channeling in which bubbles tend to collapse into the middle of the testbed. The pictures of the 3D visual display in the top of Figure 5.3 show such channeling behavior for BIF values at 3.5, 6.5 and 9.5 Hz.

To carry out the POD analysis, a 22×70 grid is used to digitize each frame in running the DIBS simulation with multiple bubble injectors. A total of 3502 frames are collected for each BIF value. This generates a data matrix of size 1540×3502 for each BIF value. Our POD analysis program is encoded in Matlab and uses a built-in routine for SVD decomposition. Figure 5.4 displays the energy distribution plots from POD decomposition for the chosen bubble injection frequencies.

Figure 5.5 shows the most dominant eight modes for the DIBS simulations with four frequencies. The modes are used, based on the POD theory, to re-construct the bubble dynamics through time series coefficients. Mathematically, all modes form a basis for the multivariate time series from the digitized dynamical process. The energy distribution plots in Figure 5.4 show at least 200 modes are required to capture 80% of the bubble energy when the frequency of injection is $f = 0.5$ Hz and at least 400 modes for $f = 3.5$, $f = 6.5$ and $f = 9.5$ Hz.

Besides the energy distribution and mode information, the main result from the POD decomposition is the time series for the temporal coefficients. Figure 5.6 shows the time series plots of the time-dependent coefficients associated with the most dominant mode, a_1, for twenty BIF values ranging from 0.5 to 10.0. This provides some insight into the overall bubble dynamics with multiple injectors since they represent the projections of the evolution over time for the bubble dynamics onto one direction of the orthogonal base.

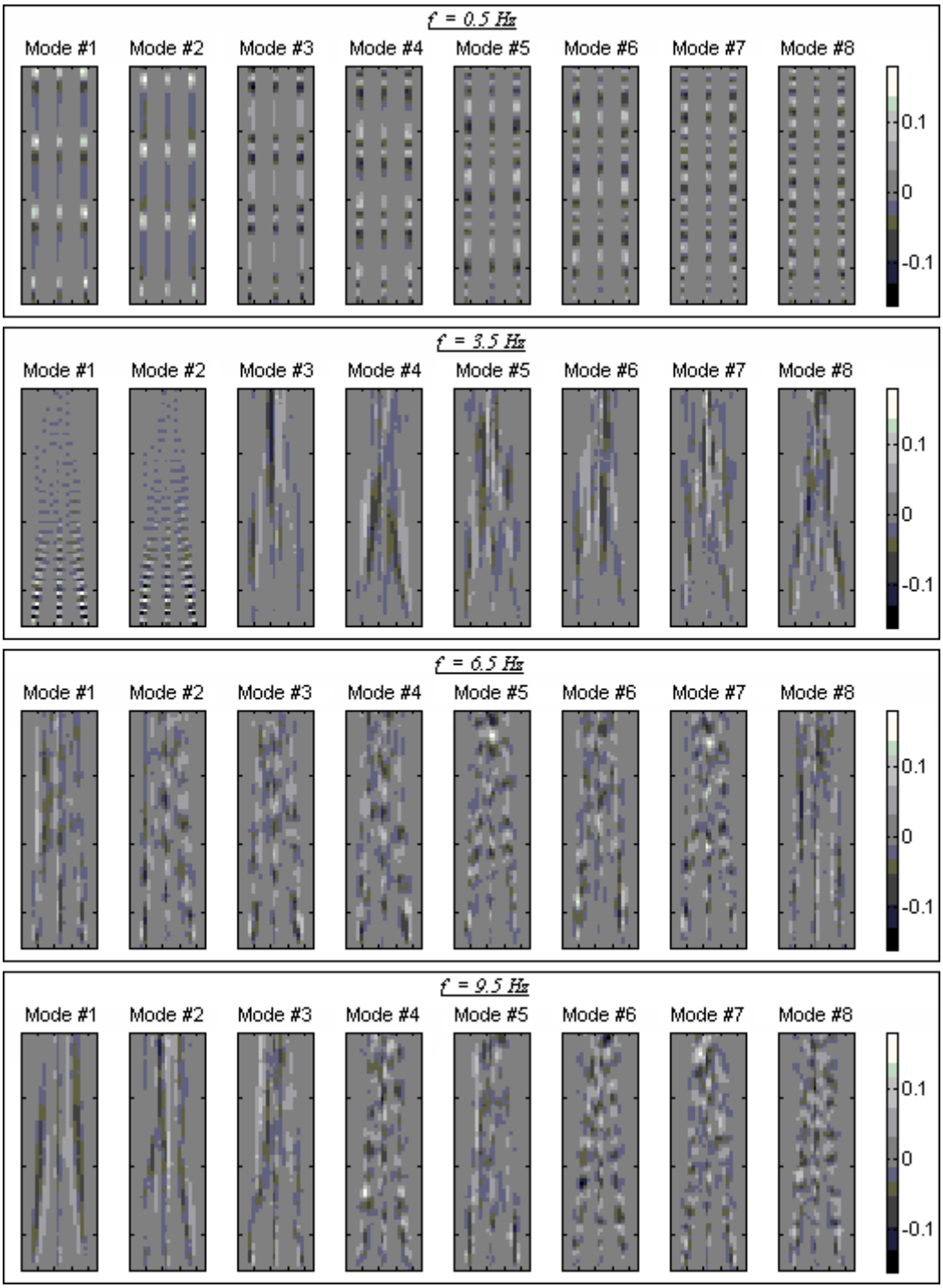

Figure 5.5: Plots of first eight POD modes of DIBS simulations with four bubble injection frequencies. All modes form an orthogonal basis.

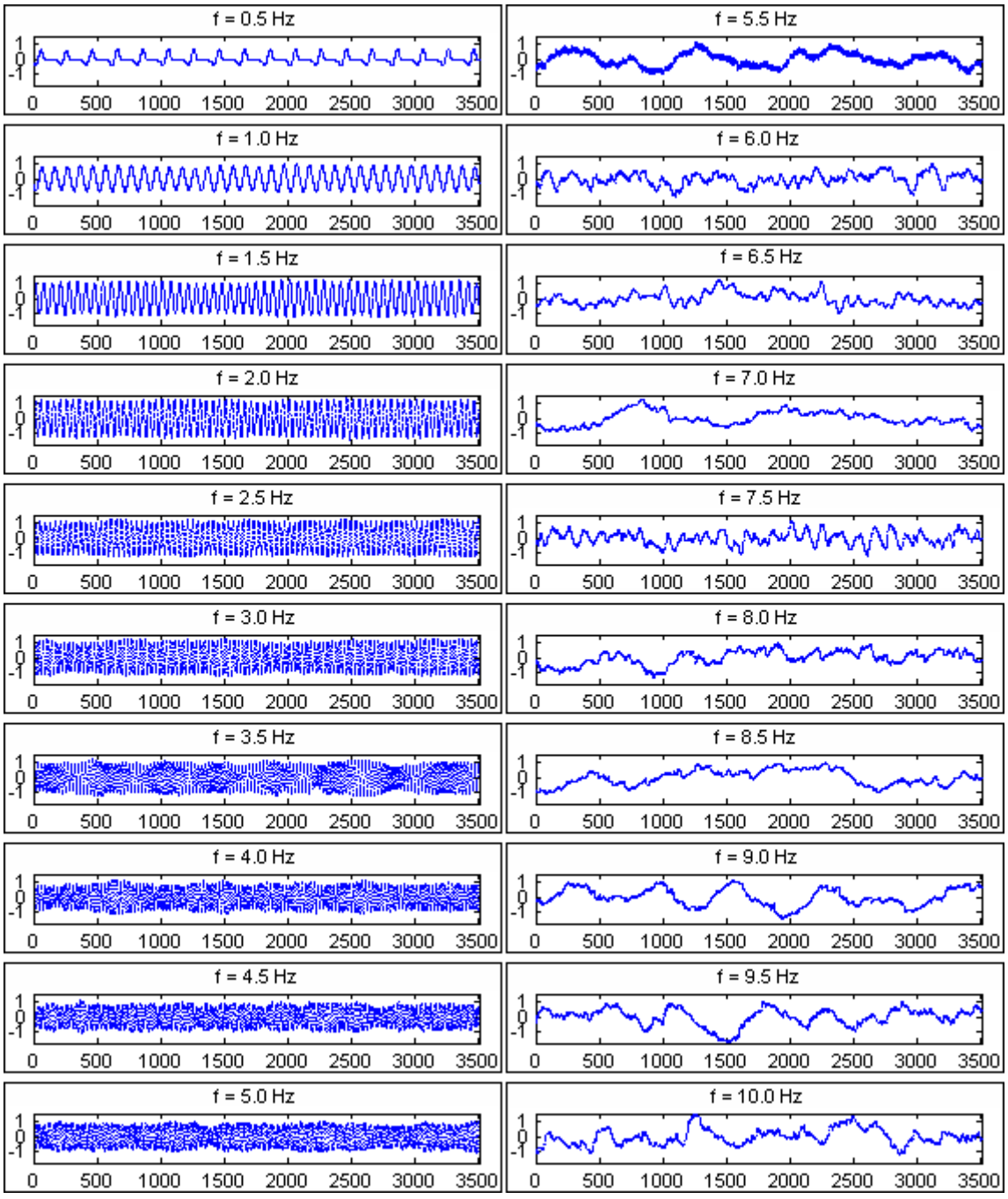

Figure 5.6: Time series plots of POD temporal coefficients for the first coefficient $a_1(t)$ from DIBS simulations with ten BIF values from 0.5 to 9.5. The time series plots reveal some transitions of dynamical behavior from a near fixed point for low BIF to complicated behavior and then to a simpler dynamics, which is similar to the case with one bubble injector.

When the BIF value is small, the time series is near constant which corresponds to a fixed point in a dynamical system. As the BIF is increased, bubbles inside the fluidized bed start to interact with each other in every possible direction. The time series plots reveal the complicated dynamical behavior when BIF is between 1.5 and 3.5. After $f = 4.5$, the system shows a less complicated behavior and then becomes gradually complicated as f increases from 6.9 Hz to 7.0 Hz. These transitions of the dynamical behaviors have indeed similarities to those in the single bubble injector case that we analyzed in Chapter 4.

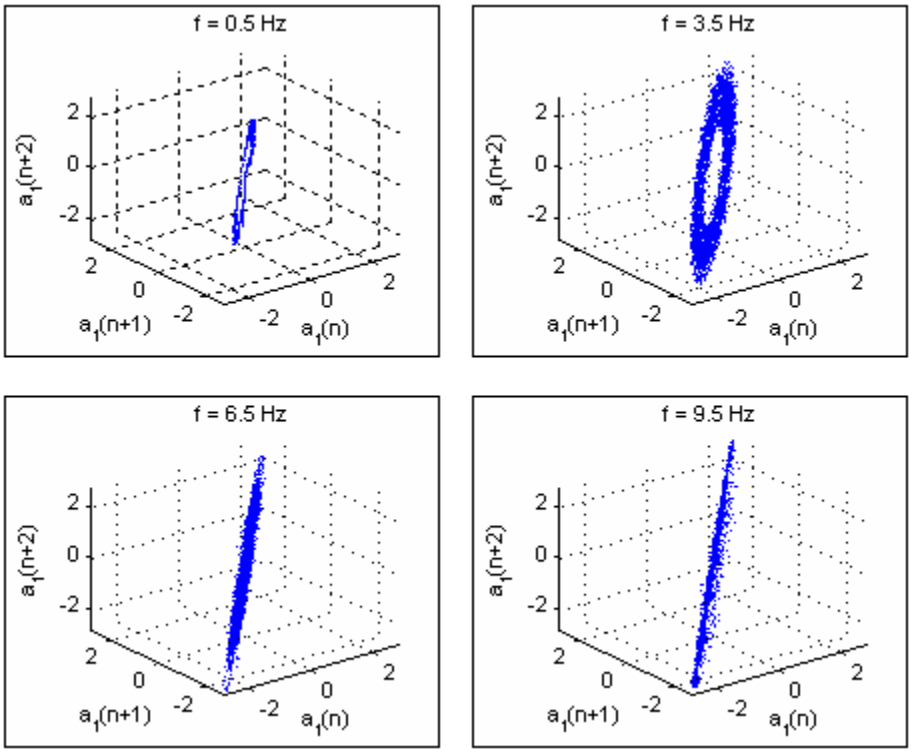

Figure 5.7: The embedding phase portraits of POD temporal data for the first coefficient, $a_1(t)$, with four different BIF values. When $f = 3.5$ Hz, a limit cycle is present from the embedded plot with embedding dimension 3.

To further understand the dynamics of the temporal evolution, techniques such as phase embedding, phase reconstruction, and model fitting, which have been described in detail in Chapter 4, can be applied. Figure 5.7 depicts phase embedding

plots of $\{a_1(t)\}$ for four chosen BIF values, which show that the existence of limit cycles for lower injection frequencies. The correlations between time evolution coefficients are also sought by constructing plots for three neighboring coefficients such as $\{a_1(t), a_2(t), a_3(t)\}$ and $\{a_2(t), a_3(t), a_4(t)\}$ in Figure 5.8 (see next page). The diagrams show clearly the existence of periodic trajectories for the first three dominant temporal coefficients.

Notice that the POD analysis is more effective when there are a few modes dominating the overall dynamics. Empirically, this is quantified as a few modes, say 20 modes, containing at least 80% of total energy. Although there are some indications of transitions of bubble dynamics from studying the time series of temporal coefficients and their correlations via POD decomposition, we realize that a direct POD decomposition still has its limitations in dealing with the case of multiple bubble injectors. This is because too many modes are needed to capture and reconstruct the original spatio-temporal dynamics. Note that the total number of vectors in the final orthogonal basis from the POD decomposition is 1540. A quick observation for the mode plots in Figure 5.5 reveals that, indeed, the POD analysis requires quite significant amount of orthogonal sub-basis to be able to reconstruct the original bubble dynamics. This will also be true for a POD decomposition of a three-dimensional discretization of bubble dynamics with multiple injectors by considering the fact that the two-dimensional projection is a subset of three-dimensional discretiziaton.

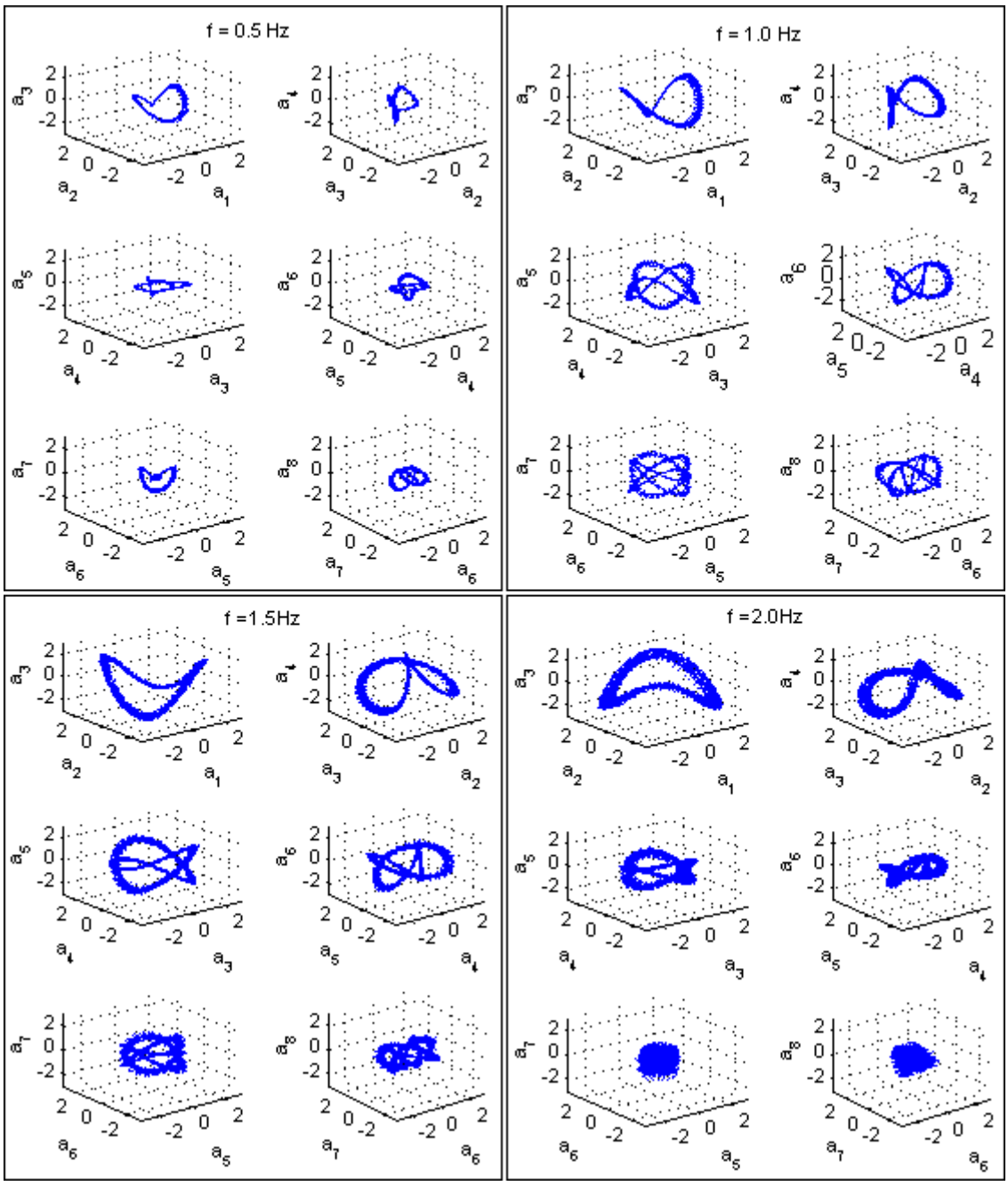

Figure 5.8: Correlations between the POD temporal coefficients are plotted for three neighboring coefficients. The diagrams show clearly the existence of periodic trajectories for the first three dominant temporal coefficients.

5.4 POD Analysis of a Spouting Bed

Spouting fluidized bed is one type of the fluidized beds that has major applications in petrochemical and metallurgic industries. When dealing with typically large particles that are difficult to fluidize with gas medium, a spouting bed is used to carry particles by a single gas jet. With a strong and sufficient gas flow, particles are entrained upward and finally rain down like a fountain. The particles then continue to move downwards until they are entrained again by the central gas jet and thus circulate in the fluidized bed for chemical reaction or heat transfer. Figure 2.2(b) in Chapter 2 depicts a schematic diagram for a spouted fluidized bed.

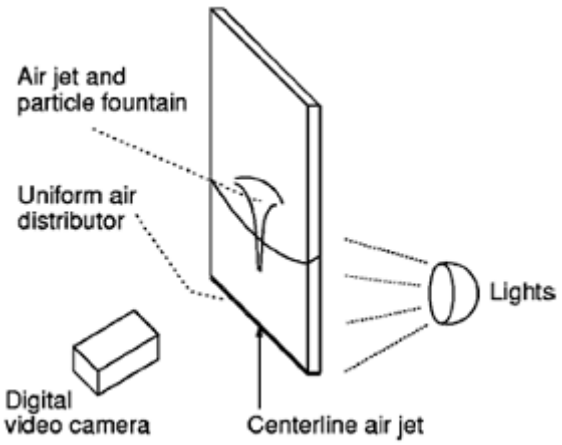

Figure 5.9: A schematic diagram of experimental spouting fluidization apparatus by Palacios *et al.* The projection of fluidization is recorded by a video camera at Oak Ridge National Laboratory for studying spouted beds.

In recent work [56], we carried out some spouting fluidized bed experiments and applied successfully the POD method for the data analysis of spouting beds. Data is actually collected by recording videos for the experiments of spouting fluidized bed.

The apparatus was constructed at the University of Tennessee for the Oak Ridge National Laboratory, including a vessel for fluidization of spherical zirshot (ZrO2), air

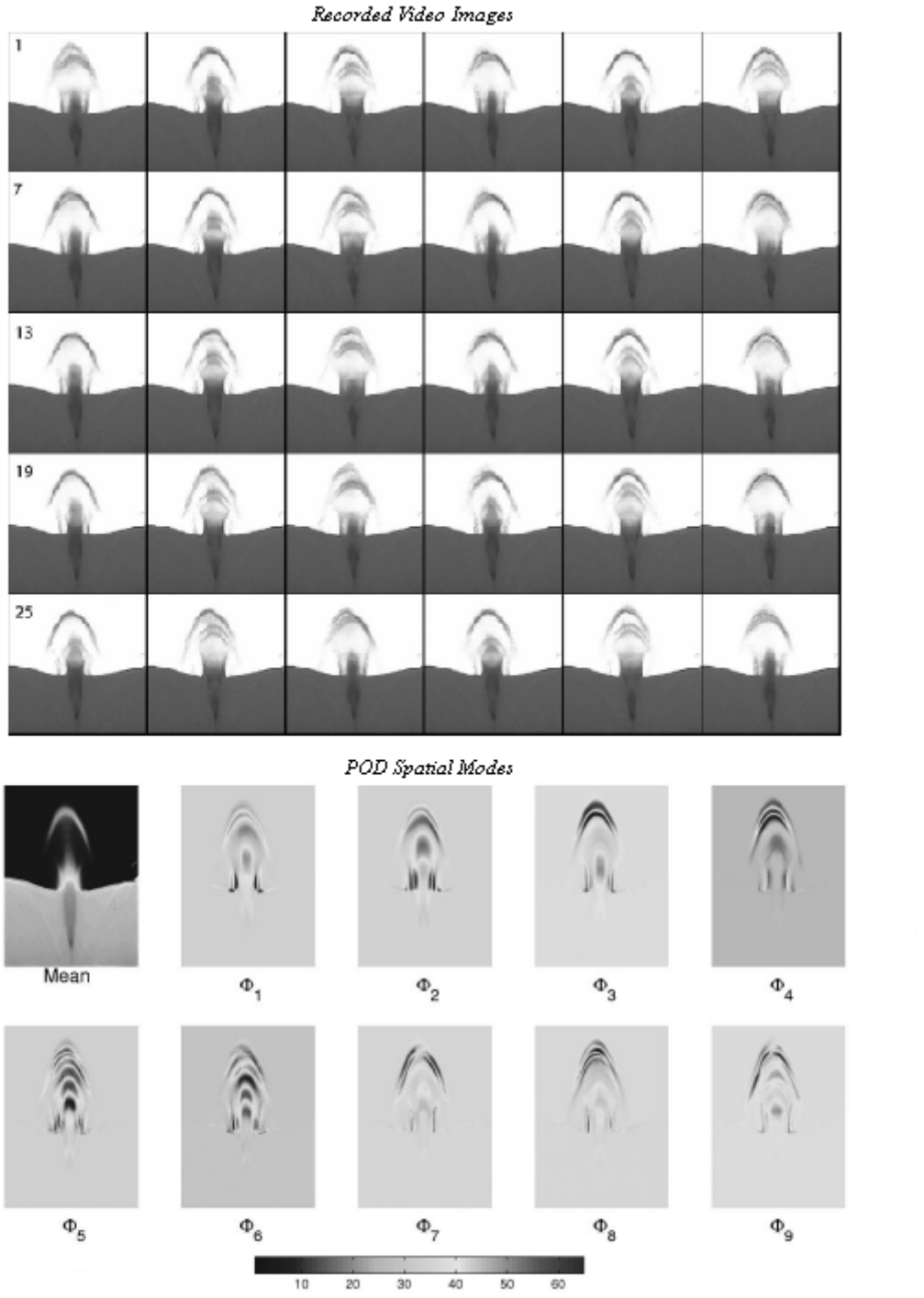

Figure 5.10: Images on the top are recorded video images for the spouting bed from experiments for jet velocity at $v = 43$ m/s. The spouting behaviors have variations. The images in the bottom portion are the POD spatial modes computed from recoded video image at same jet velocity. The first 20 modes contribute the 80% of the jet fluidization behavior.

jet nozzle, lights and digital video camera (Figure 5.9). The flowing medium in the experiment is the air that is regulated to pass through a sintered-metal distributor. A central nozzle is placed in the vessel centerline and the controlled flow air passes through the nozzle to create a fluidized bed. The jet velocity of the central nozzle is adjustable as the experimental parameter. For the experiments, velocities are chosen between 23 and 43 m/s. The top images in Figure 5.10 form a montage of video frames for the spouting bet experiment with jet velocity at 43 m/s. A closer look reveals each image has its own variations, indicating there is no steady state.

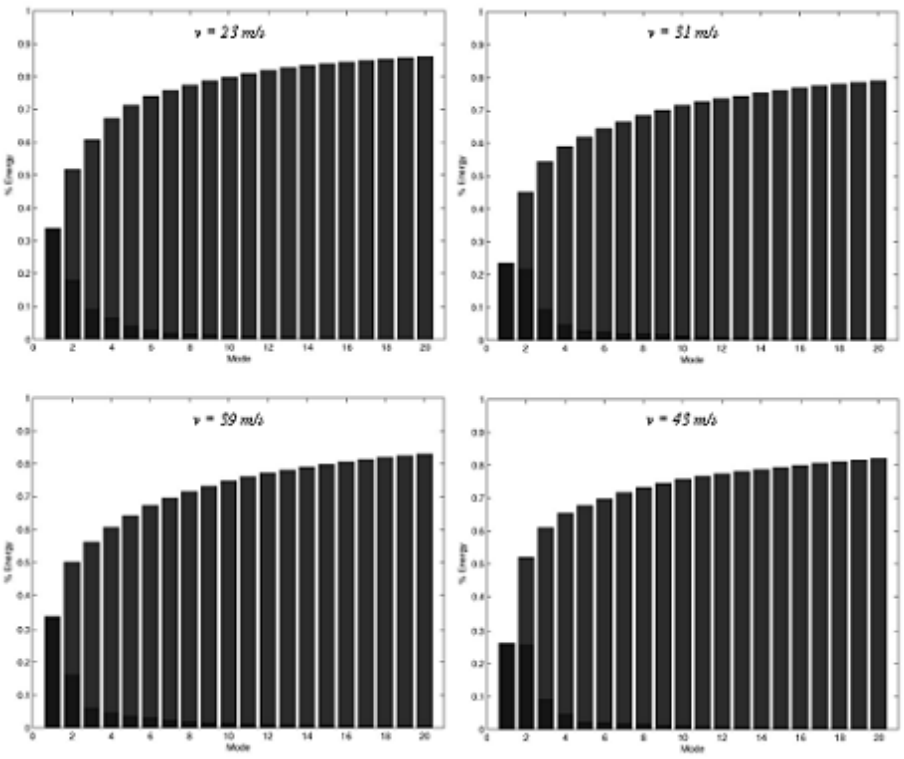

Figure 5.11: Energy distribution plots up to first 20 modes from POD analysis on the spouting bed with jet velocities at $v = 23$, $v = 31$, 39, and 43 m/s. All of them shows first 20 modes contain 80% of total energy.

From the experiments with various jet velocities, the POD analysis shows that 20 modes are sufficient to capture 80% of the total fluidization behavior. Figure 5.11 shows the energy spectrum for the first 20 modes from POD analysis for jet velocity

$v = 43$ m/s. The plot also shows that first two modes contain about 25% of POD energy. Obviously, the higher energy modes contribute more to the jet and gas-particle interaction. The images in the bottom portion in Figure 5.10 are the plots of the first nine spatial modes for the same jet velocity. Other mode plots reveal that low energy modes also contribute to the fluidization behavior located near the bed surface.

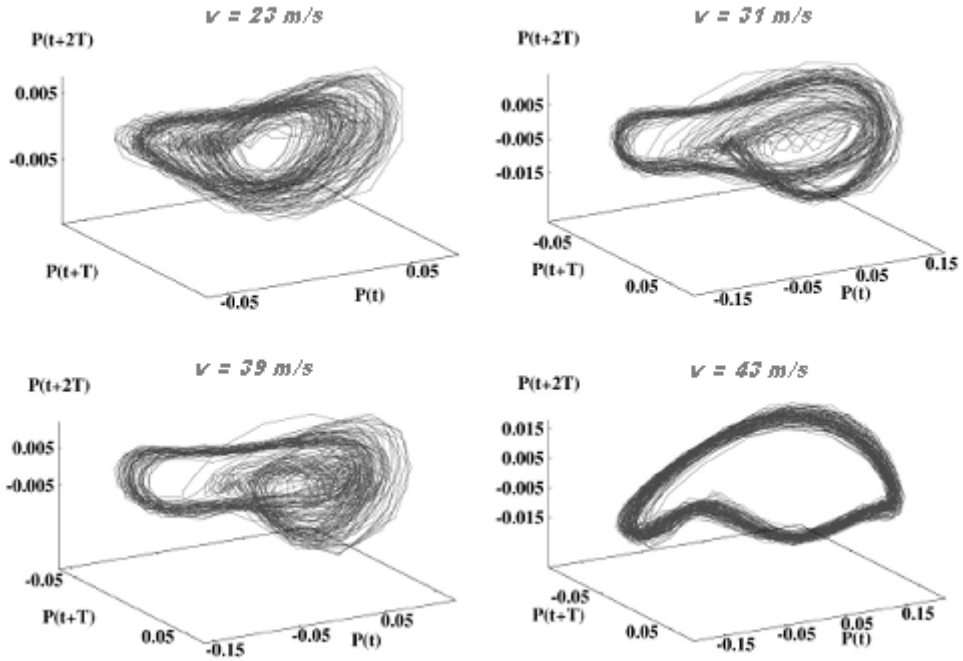

Figure 5.12: The embedding phase plots of measured pressure data for four jet velocities at $v = 23$, 31, 39, 43 m/s. The existence of low-dimensional periodic behavior in which a period-doubling bifurcation appears to occur as jet velocity decreases.

Besides the video images, the pressure inside the spouting bed is also measured and a Poincaré map is constructed based on the collected time series of pressure data. Figure 5.12 displays four embedding plots for pressure data with jet velocity at $v = 23$, 31, 39 and 43 m/s. The plots reveal the existence of low-dimensional periodic trajectory that undergoes a period-doubling bifurcation as the jet velocity decreases.

The success of separating dominant spatial data and temporal evolution data

suggests the possibility of reconstructing the low-dimensional dynamics via Galerkin projections from an originally PDE model of three-phase gas-solid-bubble system onto the POD modes. This task is not, however, part of this thesis project.

Chapter 6

Emulsion Phase Dynamics

6.1 Computational Simulations

As described earlier in Section 2.3, flowing gas and fine particles form the emulsion phase in a fluidized bed. Bubbles that move vigorously upward impact the motion of emulsion phase and vice versa. Thus it would be realistic to include the interactions between bubble phase and emulsion phase into the computational model. When using Eulerian approach for all phases in a fluidized bed, the coupling function that models interactions among different phases is included in the governing equations. For the Eulerian-Lagrangian approach, in which a discrete mode is used to trace bubbles such as the DIBS model and Kuipers' DBM model, the coupling function between bubbles and emulsion phase is not obvious. We explain this point in more detail next.

As mentioned in Section 3.2.1, the emulsion phase is affected by bubble phase through the calculation of volume fraction in both the continuity equation and the Navier Stokes equation, for both DIBS and DBM model. This is only a one-way coupling. Regarding the influence of emulsion phase over bubble phase, the DBM approach by Kuipers *et al.* [7] indicates that the emulsion phase affects the bubble force balance of bubbles through the slip velocity and virtual mass force. Thus the

DBM model, a Newtonian approach in modeling bubbles, is truly two-way coupled with emulsion phase.

For our DIBS model, a straightforward approach can be derived to describe the impact of emulsion phase on bubbles. As described in Section 3.2.2, we present a simplified one-dimensional case, in which a fluidized bed is discretized into slices in the vertical direction to compute the averaged velocities of emulsion phase in each slice. Since bubbles in a fluidized bed move upward mainly due to buoyancy force, the motion of emulsion phase will certainly affect bubble movement. Note that assumption (vii) for the DIBS model in Section 3.1.2 has not been used when performing computational DIBS simulations. The two-way coupling for both bubble phase and emulsion phase can be realized by modifying the formula for actual bubble rise velocity in the vertical direction with the emulsion velocities obtained from solving the one-dimensional continuity equation. Thus the bubble velocity can be adjusted by:

$$u_{b,x} = v_{i,x} \tag{6.1}$$

$$u_{b,y} = v_{i,y} \tag{6.2}$$

$$u_{b,z} = v_{i,z} - u_{emul}, \tag{6.3}$$

where, referring to Figure 3.3, $v_{i,x}$, $v_{i,y}$, and $v_{i,z}$ are axial projections of bubble rising velocity from Eq. (3.8), $u_{b,x}$, $u_{b,y}$, and $u_{b,z}$ are actual bubble velocities in x, y, z directions. u_{emul} is the emulsion velocity and is computed through our continuity equation using finite difference method through Eq. (3.15) in Chapter 3. This two-way coupling method was established independently during a project discussion by Sreekanth Pannala at Oak Ridge National Laboratory, A. Palacios and P. Blomgren at San Diego State University, and myself in December 2007. It was later found that this method was first described by S. Godo [33] *et al.* in 2004. However, Godo used a different bubble velocity model by Lapin *et al.* as was mentioned in Chapter 3.

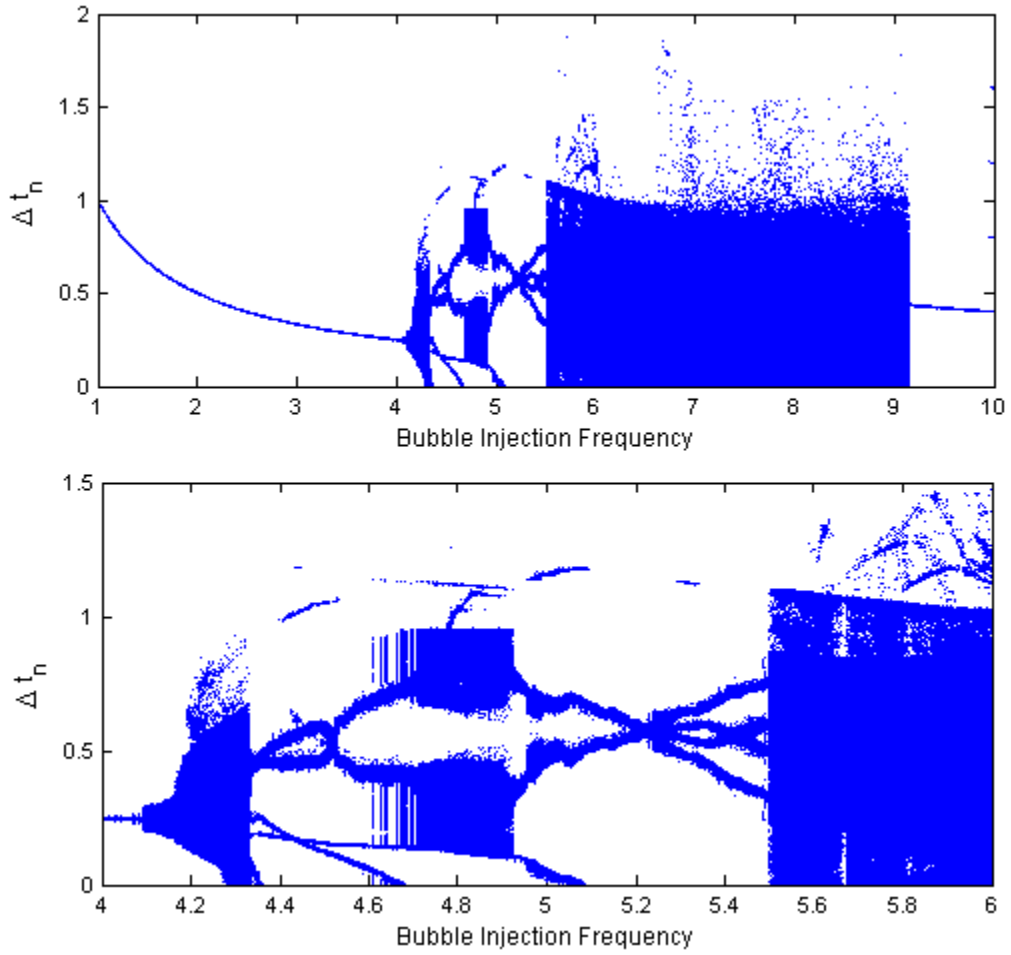

Figure 6.1: Bifurcation diagrams of revised model with coupled bubble and emulsion phases. The edges along attractors and periodic solutions are smoothed out. four attractors in the area between $f = 4.72$ and $f = 4.86$ Hz are collapsed into two attractors.

6.2 Bifurcation Analysis with Revised Model

With two-way coupling between bubble and emulsion phases, the bifurcation analysis in previous chapters is expected to undergo some changes. We start again with the case of a single injector, in which case the changes of bubble dynamics is expected to be small since there is only a single stream of bubbles.

Figure 6.1 is a reconstructed bifurcation diagram for the time series of the time

intervals between two passing bubbles, $\{\Delta t_i\}$ (see Section 4.4.1). In general, the bifurcation diagram seems to be close to the one in Figure 4.3. This is expected since the bubbles with single injector in the testbed should have very limited impact on emulsion phase. But detailed analysis shows some subtle changes after bubbles are coupled with the emulsion phase. Compared with the bifurcation diagrams in Figure 4.3 and 4.4(a), the edges along attractors and periodic solutions are smoothed out, four attractors in the area between $f = 4.72$ and $f = 4.86$ Hz are collapsed into two attractors, and a better single-period solution appears for frequencies between $f = 9.12$ and $f = 10$ Hz.

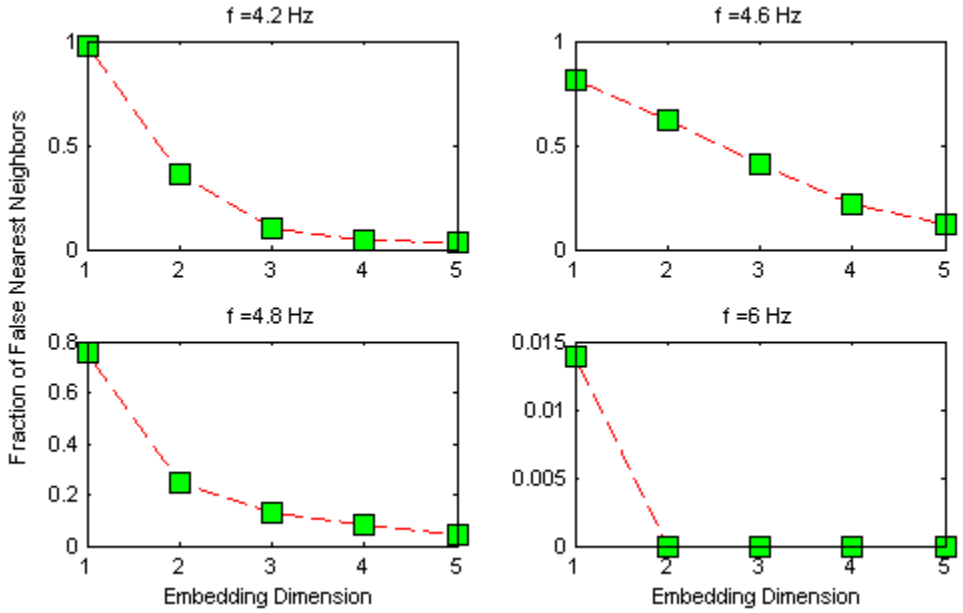

Figure 6.2: Embedding Dimensions for Revised Model. The plots show the results using the false nearest neighbor algorithm. From the plots, it can be concluded empirically that $d = 3$ for $f = 4.2$ and $f = 4.8$ Hz, $d = 5$ for $f = 4.6$ Hz and $d = 2$ for $f = 6.0$ Hz.

To obtain the embedding dimension, the FNN method described in Section 4.4.2 is once again applied to evaluate the fractions of false nearest neighbors for chosen BIF values at $f = 4.2$, $f = 4.6$, $f = 4.8$ and $f = 6.0$ Hz, and the results are plotted in

Bubble Injection Frequency (Hz)	4.2	4.6	4.8	6.0
d (original DIBS)	3	3	3	–
d (revised DIBS)	3	3	4	2

Table 6.1: Comparison of embedding dimensions for four chosen BIF values between the original DIBS model and the revised DIBS-emulsion model.

Figure 6.2. From the plots, the embedding dimensions can be empirically concluded to be $d = 3$ for $f = 4.2$ and 4.8 Hz, $d = 5$ for $f = 4.6$ Hz, and $d = 2$ for $f = 6.0$ Hz. With these results, the local linear fitting routine, *nstep*, is employed to compute the predicted trajectories for these four BIF values. For $f = 4.2$ Hz and $f = 4.6$ Hz, the local linear fitting routine works well with the embedding dimensions of 3. Although the embedding dimension for $f = 4.8$ appears to be 3, the linear fitting routine failed to create predicted trajectories. But it works better when d is chosen to be $d = 4$. For $f = 6.0$ Hz, the linear fitting works well with expected $d = 2$ based on the corresponding FNN plot in Figure 6.2. Table 6.1 lists the changes in embedding dimensions between the original DIBS simulations and the revised DIBS-emulsion model.

The results of simulation data with the revised DIBS model and the predicted simulation data are plotted in Figure 6.3 in green and in black, respectively, for the same selected BIF values. Note that, at $f = 4.8$ Hz, the predicted data is actually created with embedding dimension $d = 4$ and the plot shows nice fit between the predicted the data and simulation data. In Section 4.4.3, we showed intermittent behavior of bubble time series and indicated that methods for future data prediction failed to work for $f > 5.55$ Hz. However, this is no longer true for the revised model. The numerical experiments and the local linear fitting method show, surprisingly, that the embedding dimension is $d = 2$, indicating an interesting change from the intermittent behavior in the original DIBS simulation for $f > 5.55$ Hz to low dimensional chaos in the revised DIBS-emulsion coupling model. The relative forecast errors for $f = 4.2$,

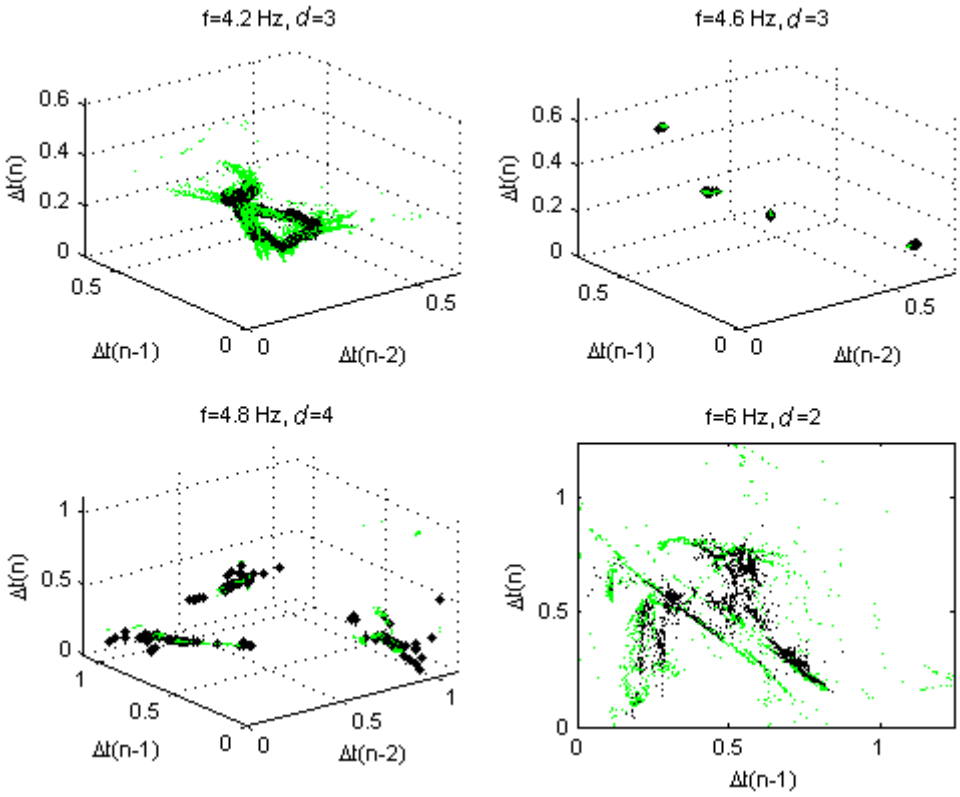

Figure 6.3: Local linear fitting model works for $f = 4.2$ with embedding dimension $d = 3$, and for $f = 6.0$ Hz with $d = 2$. It works, however, for $f = 4.8$ Hz only when the embedding dimension is $d = 4$. The original bubble data is plotted in green while the predicted trajectories are in black.

$f = 4.6$, $f = 4.8$, and $f = 6.0$ Hz are 0.246, 0.007, 0.009, and 0.55, respectively.

6.3 Ozone Concentration

In an ozone fluidized bed reactor, the flowing medium is gas containing ozone. As ozone enters the fluidized bed uniformly from the bottom, certain amount of ozone is decomposed through interactions with catalyst, sand particles, and then is converted into oxygen in the emulsion phase during the fluidization process.

In practice, each bubble in an ozone fluidized bed contains little solids while the

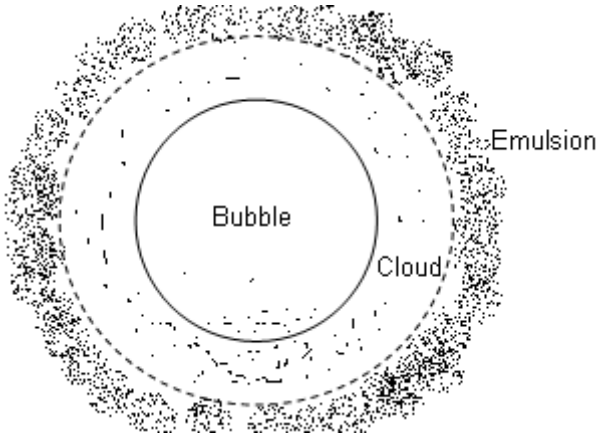

Figure 6.4: A schematic diagram of bubble, cloud and emulsion.

wake of a bubble has a significant amount of solids. There is a region, called cloud, between a bubble and its surrounding emulsion phase as is illustrated in Figure 6.4. In 1991 Kunii and Levenspiel [45] developed the following mass transfer correlations.

$$\frac{1}{K_{BE}} = \frac{1}{K_{BC}} + \frac{1}{K_{CE}}, \tag{6.4}$$

$$K_{BC} = Q/V = \frac{4.5U_{mf}}{D} + \frac{5.85D_G^{0.5}g^{0.25}}{D^{1.25}}, \tag{6.5}$$

$$K_{CE} = 6.78(\varepsilon_{mf}D_G u_b D^{-3})^{0.5}, \tag{6.6}$$

where K_{BE} is the overall gas exchange coefficient between bubble and emulsion, K_{BC} is the exchange coefficient between bubble and cloud, K_{CE} is the exchange coefficient between cloud and emulsion, D is the diameter of the bubble, D_G is the gas diffusion coefficient, ε_{mf} is the void fraction at minimum fluidization, and u_b is the bubble velocity.

The ozone concentration at the exit of a bed for each exiting bubble is computed at each time point that is multiples of initial time step size, namely, $n \cdot \Delta t$ for $n = 1, 2, 3, ...$ Then the following formula is used to evaluate ozone concentration for all

exiting bubbles:

$$c_{exit} = \frac{\sum_{exiting-bubbles} (V_{bub} \cdot c_{bub,i}) + U_{mf} \cdot \Delta t \cdot A_{bed} \cdot c_{bed,exit}}{\sum_{exiting-bubbles} V_{bub} + U_{mf,new} \cdot \Delta t \cdot A_{bed}}, \tag{6.7}$$

where c_{exit} is the ozone concentration at the exit of the bed, V_{bed} is the bubble volume, $c_{bub,i}$ the ozone concentration in the *i-th* exiting bubble, $U_{mf,new}$ is the corrected minimum fluidization, and A_{bed} is the area of the bed. Finally the averaged ozone concentration forms one data point for a given gas superficial velocity in Figure 6.5.

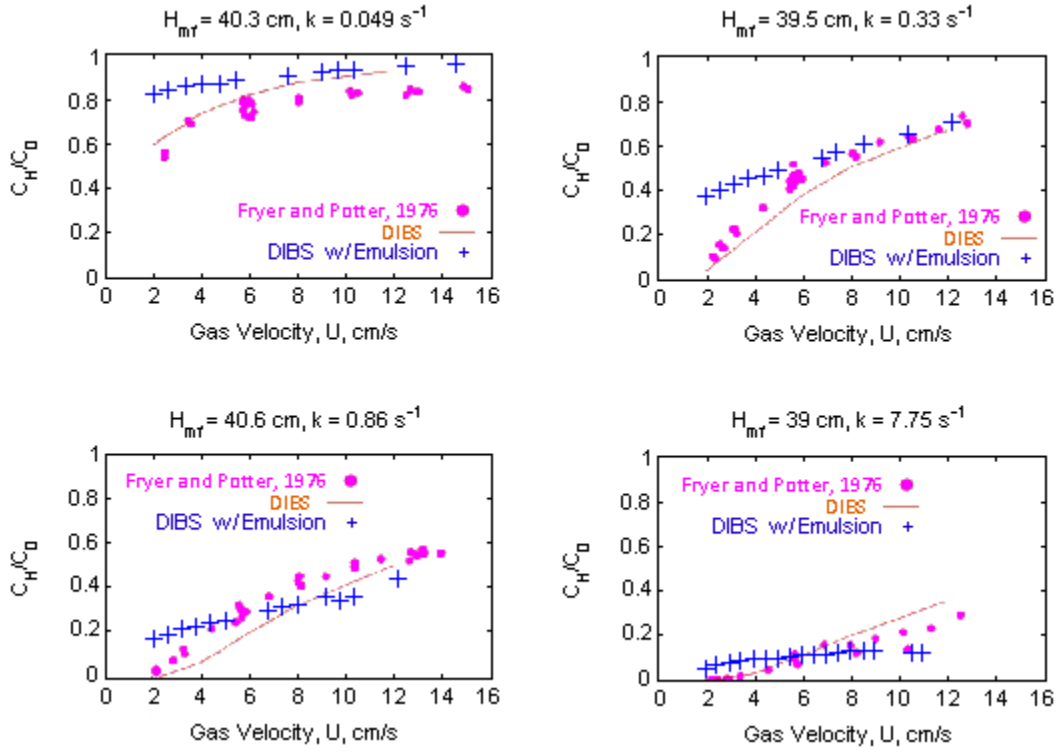

Figure 6.5: Comparison of ozone concentrations at outlet with four sets of configurations of bed height (H_{mf}) at minimum fluidization and reaction rate of ozone decomposition (k). The computational results demonstrate fairly good match with the data from actual experiments, especially for the cases with large gas velocities.

For calculating ozone concentrations, the initial size of each new formed bubble is determined with the two-phase model, *i.e.*, based on the difference between the gas

superficial velocity and minimum fluidization velocity. This is slightly different from the simulations in previous bubble bifurcation analysis in which initial bubble size is to be chosen with a predefined fixed size.

We ran the simulations by varying the gas (superficial) velocities, the reaction rates for ozone decomposition, and the bed initial heights, along with other configurations used by Fryer and Potter [29] and compared results among three approaches: measured results from the actual experiments carried by Fryer and Potter in 1976, computational results using the original DIBS model by Pannala in 2003, and our results using a revised DIBS model. Figure 6.5 shows the plots for the simulations with four sets of initial values.

When gas velocity is low, the revised DIBS-emulsion model shows significant difference in ozone concentrations compared to those obtained by Fryer and Potter. In particular, the revised DIBS model appears to show higher concentrations for low velocities. As gas velocity increases, the computational results demonstrate fairly good match with the data from actual experiments. This suggests that further tuning of the rules that make up of the DIBS model may be necessary.

Chapter 7

Conclusions and Future Work

Using a low-dimensional, agent-based bubble DIBS model, rising bubbles in a fluidized bed are simulated computationally in modern computers, including important realistic bubble-bubble interactions, coalescence of bubbles and bubble-bubble trailing effect. We identified the passage time of successive bubbles through a fixed observation point as a measurement variable to describe the spatio-temporal behavior of bubbles. Also, we investigated the bifurcations of global bubble dynamics in response to changes in a distinguished bifurcation parameter, the bubble injection frequency. Our research reveals that the global dynamics exhibits complicated behavior that undergoes a series of bifurcations, as the injection frequency increases, including fixed points, highly periodic orbits, chaotic attractors, and intermittent behavior. Aided by time series analysis, we were able to approximate nonlinear models through phase-space embedding and local linear fitting methods that reconstruct significantly well the global dynamics except in regions where the system shows intermittency. Our approach to find computational estimates of maximum Lyapunov exponents succeeded at most frequency points and showed consistent results with the associated bifurcation diagrams. More importantly, the exponents confirm the presence of low-dimensional deterministic chaos in the evolution of the bubbles.

The DIBS model addresses prevalent bubble-bubble interactions of coalescence and bubble-bubble trailing effects. The DIBS model is sufficient for modeling bubbles in a fluidized bed with fine particles. When dealing with large particles, it might be more realistic to include bubble splitting. This will be an interesting area for future research.

We presented a method to digitize bubble dynamics and employed proper orthogonal decomposition to have spatial and temporal decompositions for collected data from bubble simulations with multiple injectors. The resulting temporal evolution data reveals the transitions of bubble dynamics in a fluidized bed with a swarm of bubbles. It was found that a significant number of POD modes, more than 200 modes, are needed to be able to capture 80% of total energy in a fluidized bed. Nevertheless, the POD analysis was successfully applied to analyze a spouting bed, in which a centralized nozzle is used to produce circulating particles. With images taken from actual experiments, the POD technique shows that 20 modes are sufficient to capture 80% of the total energy of the system.

We also presented a revised model for the computational simulation of emulsion phase, which includes two-way coupling with the DIBS bubble model. In this revised model, our bifurcation analysis showed similar behaviors of global dynamics in most regions, but also some subtle differences in the embedding dimensions were obtained via time series analysis. With the revised model and an appropriate mass-transfer model, we were able to simulate some key features such as ozone concentration in a bubbling fluidized bed. The results demonstrate good agreement, especially for large gas velocities. The simulations, however, are currently based on a simplified one-dimensional numerical approach for the emulsion phase, which is suitable for the case of a single bubble injector. In reality, the emulsion phase often has circulated motion that can not be described by a one-dimensional approach. We expect the results of

this thesis can be improved when a complete three-dimensional solution of emulsion phase is incorporated into the DIBS simulation with multiple injectors. This task is, however, part of future work.

Bibliography

[1] S. A. Allahwala. Computer Simulation of Bubble Behaviour in Three Dimensional Fluidised Beds. Ph.D. dissertation. Monash University, 1975.

[2] K. T. Alligood, T. D. Sauer and J. A. Yorke. Chaos: an introduction to dynamical systems. Springer-Verlag New York, Inc, (1996).

[3] M. Behling and D. Mewes. X-ray computational tomography measurement of 3-phase flow in bubble columns. Bubbly Flows: analysis, modeling and calculation. Springer-Verlag, 233-241, 2004.

[4] T. Blake and P. Chen. Computer Modeling of Fluidized Bed Coal Gasification Reactors. American Chemical Society Symposium Series 168, 157-183 (1981).

[5] C. M. van den Bleek and J. C. Schouten. Deterministic Chaos: A new tool in fluidized bed design and operation. Chem. Eng. J. 53. 75-87 (1993).

[6] P. Blomgren, *et al.* Bifurcation Analysis of Bubble Dynamics in Fluidized Beds. Chaos 17, 013120 (2007).

[7] G. A. Bokkers, J. A. Laverman, M. van Sint Annaland, J. A. M. Kuipers. Modeling of large-scale dense gas-solid fluidized beds using a novel discrete bubble model. Chem. Eng. Sci. 61, 5590-5602 (2006).

[8] Oliver Borchers and G. Eigenberger. Detailed experimental studies on gas-solid bubble flow in bubble columns with and without recycle. Bubbly Flows: analysis, modeling and calculation. Ed. Martin Sommerfeld. Springer-Verlag, 1-10, 2004.

[9] J. Buhl, D. J. T. Sumpter, I. D. Couzin, J. J. Hale, E. Despland, E. R. Miller, S. J. Simpson. From disorder to order in marching locusts. Science 312, 1402-1406 (2006).

[10] H. Caram and K. Hsu. Bubble Formation and Gas Leakage in Fluidized Beds. Chem. Engng. Sci. 41(6), 1445-1453 (1986).

[11] George. G. Chase. Solids Processing. Online September, 2007.

[12] R.C. Chen, L. S. Fan. Particle Image Velocimetry for Characterizing the Flow Structure in Three-Dimensional Gas-Liquid-Solid Fluidized Beds. Chem. Eng. Sci., 47, 3615 (1992).

[13] Nicholas Cheremisinoff and P. Cheremisinoff. Hydrodynamics of Gas-Solids Fluidization. Golf Publishing Company, Houston, 194-95, 1984.

[14] R. Clift and J. R. Grace. Bubble Interaction in Fluidized Beds. Chem. Eng. Prog. Symp. Ser. 66, 14, (1970).

[15] J.F. Davidson, R. Clift, D. Harrison. Fluidization. 2nd ed. Academic Press, London, (1985).

[16] R. M. Davies and G. I. Taylor. The mechanics of large bubbles rising through extended liquids and through liquids in tubes. Proc. R. Soc. London A 200, 375 -390 (1950).

[17] C.S. Daw and J.S. Halow. Evaluation and control of fluidization quality through chaotic time series analysis of pressure-drop measurements. AIChE Symp. Ser. 89, 103-122 (1993).

[18] C.S. Daw and J.S. Halow. Modeling deterministic chaos in gas fluidized beds. AIChE Symp. Ser. 88, 61-69 (1992).

[19] C.S. Daw, C.E.A. Finney, M. Vasudevan, N.A. van Goor, K. Nguyen, D.D. Bruns, E.J. Kostelich, C. Grebogi, E. Ott, and J.A. Yorke. Self-organization and chaos in a fluidized bed. Phy. Rev. Lett. 75, 2308-2311 (1995).

[20] C. S. Daw, S. Pannala, and J. S. Halow. Simulations of Reacting Fluidized Beds Using an Agent Based Bubble Model. Proceedings of Chemical Reaction Engineering IX; Chemical Reactor Engineering - Meeting the Challenges For New Technology, Quebec City, Quebec, Canada, June 29-July 4, 2003.

[21] C. S. Daw, W. F. Lawkins, D. J. Downing, and N. E. Clapp Jr. Chaotic Characteristic of a Complex Gas-solid Flow. Phys. Rev. A 41, 1179-1181 (1990).

[22] N. G. Deen, M. van Sint Annaland, J. A. M. Kuipers. Multi-scale modeling of dispersed gas-solid two-phase flow. Chem. Eng. Sci. 59, 1853-1861(2004).

[23] J. -P Eckman, S. Oliffson Kamphorst, D. Ruelle, and S. Ciliberto. Lyapunov exponents from a time series. Phys. Rev. A 34, 4971(1986).

[24] L. S. Fan. Bubble Dynamics in Liquid-Solid Suspensions. Developments in Fluidization and Fluid Particle Systems. AIChe Symposium Series, No. 308. Volume 91, 1995.

[25] L.S. Fan and C. Zhu. Principles of Gas-Sold Flows. Cambridge University Press, New York, 1998.

[26] J. D. Farmer and J. Sidorowich. Predicting chaotic time series. Phys. Rev. Lett. 59, 845 (1987).

[27] T. Farrokhalaee and R. Clift. Mechanistic Prediction of Bubble Properties in Freely-bubbling Fluidized Beds. Proceedings of the 1980 International Fluidization Conference, pp. 135-142, Henniker, New Hampshire, 1980.

[28] Fluidization. http://en.wikipedia.org/wiki/Fluidization. Online September, 2007.

[29] C. Fryer and O. Potter. Experimental Investigation of Models for Fluidized Bed Catalytic Reactors. AIChE Journal, 22, 38-47, (1976).

[30] S. Garg and J. Prichett. Dynamics of Gas-fluidized Beds. Journal of Applied Physics 46, 4493-4500 (1975).

[31] D. Gidaspow. Multiphase Flow and Fluidization. Academic, Boston, 1994.

[32] D. Gidaspow and B. Ettehadieh. Fluidization in two-dimensional beds with a jet; part 2: Hydrodynamic modeling. Ind. Eng. Chem. Fundam. 22, 193-201(1983).

[33] S. Godo *et al.* Dynamics of the Flow in Bubble Column Reactors. Bubbly Flows: analysis, modeling and calculation. Ed. Martin Sommerfeld. Springer-Verlag, 53-65, 2004.

[34] J.S. Halow and O. Nicoletti. Observation of fluidized bed coalescence using capacitance imaging. Powder Technology, 69 (1992) 255-277

[35] J. S. Halow, G. Fasching, P. Nicolletti and J. Spenik. Observations of a Fluidized Bed Using Capacitance Imaging. Chemical Engineering Science, Vol. 48, No. 4, pp. 643-659, 1993.

[36] D. Harrison and L. Leung. Bubble Formation at an Orifice in a Fluidized Bed. Trans. Instn. Chem. ENgre. 39, 409-414 (1961).

[37] R. Hegger, H. Kantz and T. Schreiber. Nonlinear Time Series Analysis. Online November 27, 2007. http://www.mpipks-dresden.mpg.de/ tisean/TISEAN_2.1.

[38] R. Hegger, H. Kantz and T. Schreiber. Practical implementation of nonlinear time series methods: The TISEAN package. Chaos 9, 413-435 (1999).

[39] S. Kaart, J. C. Schouten, and C. M. van den Bleek. Improving conversion and selectivity of catalytic reactions in bubbling gas-solid fluidized bed reactors by control of the nonlinear bubble dynamics. Catal. Today 48, 185-194 (1999).

[40] H. Kantz. A robust method to estimate the maximal Lyapunov exponent of a time series. Phys. Lett. A, 185, 77.

[41] H. Kantz and T. Schreiber. Nonlinear Time Series Analysis. Cambridge University Press. Cambridge (1997).

[42] K. Karhunen. Zur Spektraltheorie Stochasticher. Ann. Acad. Sci. Fenn., SerA 1, 34 (1946).

[43] M. B. Kennel, R. Brown, and H. D. I. Abarbanel. Determining Embedding Dimension for phase-space reconstruction using a geometrical construction. Phys. Rev. A 45, 3403 (1992).

[44] R. J. de Korte, J. C. Schouten, and C. M. van den Bleek. Controlling bubble coalescence in a fluidized-bed model using bubble injection. AiChe J. 47, 851-860 (2001).

[45] D. Kunii and O. Levenspiel. Fluidization Engineering 2nd ed. Butterworth-Heinemann, Boston (1991).

[46] M. Kwauk. Exploring the Multi-Phase Nature of Fluidization. Fluidization and Fluid Particle Systems: Recent Research and Development. AIChe Symposium Series, No. 318, Volume 94, 1998.

[47] A. Lapin et al. Industrial-scale bubble column reactors: gas-liquid flow and chemical reaction. Chem. Eng Sci., 56, 239-246, 2001.

[48] M. Loeve. Probability Theory. Van Nostran, New York, 1955.

[49] W. K. Lord. Bubbly Flow in Fluidized Beds f Large Particle. Sc.D. thesis, Department of Mechanical Engineering, MIT, Cambridge, 1983.

[50] L. Massimilla, A. Solimando, and E. Squillace. Gas Dispersion in Solid-Liquid Fluidised Beds. British Chemical Engineering, 6, 232 (1961).

[51] Navier-Stokes equations. Online October 18, 2007. http://en.wikipedia.org/wiki/Navier-Stokes_equation.

[52] A. Nguyen, A. Fletcher and J. Tu. CFD Study of the Heat Transfer between A Dilute Gas Particle Suspension Flow and an Obstruction. Numerical Heat Transfer, Part A: Applications, 35:5, 537-551, 1999.

[53] K. Nguyen, P. Chakka, M. Cheng, C. E. A. Finney, D. D. Bruns, C. S. Daw, and M. B. Kennel. Spatio-temporal dynamics in a train of rising bubbles. Chem. Eng. J. 64, 191-197 (1996).

[54] J. Nieuwland, M. Veenendaal, J. Kuipers, and W. Vanswaaij. Bubble Formation at a Single Orifice in Gas-fluidized Beds. Chem. ENgng. Sci. 51(17), 4087-4102 (1996).

[55] J. C. Orcutt and B. H. Carpenter. Chem. Eng. Sci. 26, 1049-1064, 1971.

[56] A. Palacios, C. Finney, P Cizmas, S. Daw and T. O'Brien. Experimental analysis and visualization of spatiotemporal patterns in spouted fluidized beds. Chaos, vol. 14, No. 2, 2004.

[57] S. Pannala, C. S. Daw, and J. S. Halow. Agent-Based Model for Bubbling Fluidized Beds. 2003 SIAM Conference on Computational Science and Engineering, San Diego, February 10-13, 2003.

[58] S. Pannala, C. S. Daw, and J. S. Halow. Dynamic Interacting Bubble Simulation (DIBS): An Agent-based Bubble Model for Reacting Fluidized Beds. Chaos, Volume 14, Number 2, June 2004.

[59] S. Pannala, C. S. Daw, and J. S. Halow. Near Real-time Simulations of Large Fluidized Beds with a Low Order Bubble Model. Session 199b, AICheE Annual Meeting, Reno, Nevada, November 4-9, 2001.

[60] S. Pannala, C.S. Daw, J. Halow. Simulations of Reacting Fluidized Beds using Agent-based Bubble Model. International Journal of Chemical Reactor Engineer. Article A20, Volume 1, 2003.

[61] Principal Components Analysis. Online December 2007. http://en.wikipedia.org/wiki/Karhunen-Lo%C3%A8ve_transform.

[62] Vivek V. Ranade. Computational Flow Modeling for Chemical Reactor Engineering. Academic Press. San Diego (2004).

[63] D. Richner, T. Minoura, J. Prichett and T. Blake. A Numerical Model of Gas Fluidized Beds. AIChE Journal, 36, 361-369 (1990).

[64] M. T. Rosenstein, J. J. Collins and C. J. De Luca. A practical method for calculating largest Lyapunov exponents from small data sets. Physica D, 65, 117.

[65] T. Sauer, J. Yorke, and M. Casdagli. Embedology. J. Stat. Phys. 65, 579 (1991).

[66] G. Schneyer, E. Peterson, P. Chen, D. Brownell and T. Blake. Computer Modeling of Coal Gasification Reactors. Technical Report DOE/ET/10247. DOE, 1981.

[67] J.C. Schouten and C.M. van den Bleek. Chaotic hydrodynamics of fluidization: consequences for scaling and modeling of fluidized bed reactors. AIChE Symp. Ser. 88, 70-84 (1992).

[68] J.C. Schouten, M.L.M. vander Stappen, and C.M. van den Bleek. Deterministic chaos analysis of gas-solids fluidization. In Fluidization (Engineering Foundation, New York, 1992), vol. VII, pp. 103-111.

[69] R. S. Shichi and I. Muchi. Interaction between Two Bubbles in Gaseous Fluidization. Kagaku Kogaku, 32, 343 (1968).

[70] L. Sirovich. Turbulence and the dynamics of coherent structures. Q. Appl. Math. 5, 561-590 (1987).

[71] D. P. Skrzycke, K.Nguyen, and C. S. Daw. Characterization of the Fluidized Behavior of Different Solid Types Based on Chaotic Time Series Analysis of Pressure Signals. Proceedings of the 12th International Conference on Fluidized Bed Combustion. San Diego, CA, 1993, pp 155-166.

[72] F. Takens. Detecting Strange Attractors in Turbulence. Lecture Notes in Math. Vol. 898, Springer, New York (1981).

[73] R. Toei and R. Matsuno. The coalescence of bubbles in the gas-solid fluidized bed, in: A.A.H. Drinkenburg (Ed.), Proceedings of the International Symposium on Fluidization. Netherlands University Press, Amsterdam, 1967.

[74] R. D. Toomey and H.F. Johnstone. Gas Fluidization of solid particles. Chem. Eng. Pro. 48, 220 (1952).

[75] Y. Tsuo and D. Gidaspow. Computation of Flow Patterns in Circulating Fluidized Beds. AIChe Journal, Vol. 36, No. 6, 1990.

[76] A. Tufaile and J. C. Sartorelli. Chaotic behavior in bubble formation dynamics. Physica A 275, 336-346 (2000).

[77] A. Tufaile and J. C. Sartirelli. Hénon-like attractor in air bubble formation. Phys. Lett. A 275, 211-217 (2000).

[78] J. Werther. Influence of the distributor design on bubble characteristic in large diameter gas fluidized beds. Fluidization - Proceedings of the 2nd Engineering Foundation Conference (J. Davidson, D. Keairns (Eds)), Cambridge University Press, Cambridge, pp. 7-12 (1978).

[79] F. Zenz. Bubble Formation and Grid Design. Instn. Chem. Engng. Symp. Ser. 30, 136-139 (1968).